Pacific Northwest
NATIONAL LABORATORY

PNNL-37144

Advanced Functional Membranes for Noble Gas Management

Fabrication and Testing of Membranes on Porous Support

December 2024

Keerthana Krishnan
Sun Hae Ra Shin
Heinirk Goettsche
Praveen K. Thallapally

U.S. DEPARTMENT OF ENERGY

Prepared for the U.S. Department of Energy
under Contract DE-AC05-76RL01830

DISCLAIMER

PACIFIC NORTHWEST NATIONAL LABORATORY
operated by
BATTELLE
for the
UNITED STATES DEPARTMENT OF ENERGY
under Contract DE-AC05-76RL01830

Printed in the United States of America

Available to DOE and DOE contractors from
the Office of Scientific and Technical Information,
P.O. Box 62, Oak Ridge, TN 37831-0062
www.osti.gov
ph: (865) 576-8401
fox: (865) 576-5728
email: reports@osti.gov

Available to the public from the National Technical Information Service
5301 Shawnee Rd., Alexandria, VA 22312
ph: (800) 553-NTIS (6847)
or (703) 605-6000
email: info@ntis.gov
Online ordering: http://www.ntis.gov

PNNL-37144

Advanced Functional Membranes for Noble Gas Management

Fabrication and Testing of Membranes on Porous Support

December 2024

Keerthana Krishnan
Sun Hae Ra Shin
Heinirk Goettsche
Praveen K. Thallapally

Prepared for
the U.S. Department of Energy
under Contract DE-AC05-76RL01830

Pacific Northwest National Laboratory
Richland, Washington 99354

Summary

We selected several porous materials including PNW-24, CC3, SAPO-34, SAPO-56 and PNW-6, as the basis for fabricating membranes for Kr/Xe separation. Initially, we synthesized powder samples of the candidates and confirmed their crystallinity and morphology with X-ray diffraction and microscopy. In the case of PNW-24 and PNW-6, we further confirmed its Xe selectivity through Xe and Kr adsorption experiments, while we relied on literature reports for CC3, SAPO-34 and SAPO-56. We subsequently proceeded to fabricate membranes on porous alumina supports using techniques such as seeded-assisted secondary growth, in-situ growth and solution-processed method. PXRD on the membranes verified that the structures were well-grown on the surface of alumina support, while SEM provided visual confirmation of particle morphology. Importantly, defects were not visually observed in the fabricated membranes, which was further verified with pressure retention tests. We analyzed the separation performance of the synthesized membranes using a dilute gas mixture comprising of xenon, krypton and argon. We focused on PNW-6 to optimize the synthesis reaction time and study the effects of time on gas separation. While more research is necessary to reach a comprehensive conclusion, in alignment with our milestones, we have successfully achieved our goals.

Acknowledgments

Acronyms and Abbreviations

APTES	aminopropyltriethoxysilane
CC3	1,3,5-triformylbenzene and (R,R)-1,2-diaminocyclohexane
DCM	dichloromethane
DI	deionized
DMF	dimethylformamide
EtOH	Ethanol
HKUST-1	Hong Kong University of Science and Technology-1
Kr	Krypton
MOF	metal-organic framework
N_2	Nitrogen
PNNL	Pacific Northwest National Laboratory
PXRD	powder X-ray diffraction
SAPO	Silicoaluminaphosphate
SASG	seeded-assisted secondary growth
SDB	sulfonyldibenzoic acid
SEM	scanning electron microscopy
TEAOH	tetraethylammonium hydroxide
Xe	Xenon
SCCM	standard cubic centimeter per minute
MS	mass spectrometer
MFC	mass flow controller

Contents

Summary ii
Acknowledgments iii
Acronyms and Abbreviations iv
1.0 Introduction 1
2.0 Identify radiation-tolerant materials 3
3.0 Powder synthesis and characterization of materials 5
3.1 PNW-24 ..... **Error! Bookmark not defined.**
3.2 PNW-6 ..... **Error! Bookmark not defined.**
3.3 CC3 7
3.4 SAPO-56 9
3.5 SAPO-34 10
4.0 Fabrication of membranes on porous support 13
4.1 Fabrication of PNW-24 membrane by seeding method 13
4.2 Fabrication of PNW-24 membrane by surface functionalization 15
4.3 Fabrication of CC3 membrane 16
4.4 Fabrication of SAPO-56 membrane 18
4.5 Fabrication of SAPO-34 membrane 18
4.6 Fabrication of PNW-6 membrane 19
4.7 Optimizing reaction time for PNW-6 membrane 21
5.0 Gas permeance testing 27
5.1 PNW-24 membrane 29
5.2 PNW-6 membrane 31
5.3 Membrane performance under dilute conditions 33
6.0 PNW-6 Membrane Simulation 36
6.1 Simulation Equations 36
6.2 Simulation Results 38
7.0 Cost Estimate 47
8.0 Challenges and future work 48
9.0 References 50

Figures

Figure 1. Energy consumption comparison for different separation methods. 1
Figure 2. Factors contributing to membrane-based separations. 2

Figure 3. (a) Xe molecule position in PNW-24 cavity determined by single-crystal X-ray diffraction; (b) the size to accommodate a single Xe molecule in CC3 cavity; (c) pore size and sodalite topology of PNW-6; (d) CHA topology of SAPO-34 (Chen et al. 2014; Banerjee et al. 2016).....4
Figure 4: Comparison of Xray diffraction patterns of synthesized PNW-24 powders with simulated pattern.....5
Figure 5: SEM images of PNW-24 powders. 5
Figure 6: Xe and Kr uptake on PNW-24 powders.....6
Figure 7: Comparison of PXRD patterns of synthesized PNW-6 crystals to the simulated pattern. 6
Figure 8: SEM image of synthesized PNW-6 crystals.....7
Figure 9: (a) Room temperature uptake of Ar, Kr and Xe on PNW-6 crystals and (b) focused isotherm on the low-pressure range.....7
Figure 10: PXRD pattern comparison of CC3 powders synthesized using solvothermal approach and room temperature approach.....8
Figure 11: SEM images of CC3 powders. 8
Figure 12. The Xe and Kr uptakes at 298 K of CC3 from literature (Chen et al. 2014). 9
Figure 13: PXRD pattern comparison of SAPO-56 seeds.....10
Figure 14: Xe and Kr isotherms on the SAPO-34 zeolites, adapted from (Feng, Zong et al. 2016) 10
Figure 15: PXRD patterns of SAPO-34 powders synthesized using different ratios of precursors in comparison to simulated pattern. 12
Figure 16: Schematic of seeding approach adapted for PNW-24 membranes. 13
Figure 17: The PXRD pattern of fabricated PNW-24 membrane with (a) simulated crystallography structure; the SEM images of PNW-24 membrane at magnifications (b) 1000X and (c) 5000X, respectively.....14
Figure 18: Membrane XRD pattern of PNW-24 membrane with different layers. 14
Figure 19: Top views (a, c, e) and cross-sectional views (b, d, f) of PNW-24 membranes synthesized using seeding approach; 3R (a, b), 4R (c, d) and 5R (e, f).....15
Figure 20: Schematic of surface functionalization approach adapted for PNW-24 membranes. 15
Figure 21: (a) Comparison of seeded PNW-24 membrane to functionalized PNW-24 membrane, (b) and (c) top view of crystals deposited on PNW-24 membrane.....16
Figure 22: CC3 in-situ room temperature membrane XRD compared with simulated pattern. 16
Figure 23: CC3 drop-casted membrane XRD compared with simulated pattern. 17
Figure 24: CC3 solvothermal membrane XRD compared with simulated pattern.....18
Figure 25: SAPO-56 membrane XRD compared with simulated pattern.....18
Figure 26: SAPO-34 membrane XRD compared with simulated pattern.....19

Figure 27: (a) Comparison of membrane XRD for PNW-6 (HC) membrane to the simulated pattern, (b) and (c) top views of the synthesized PNW-6 membrane. 20
Figure 28: Intercrystallite defects created as seen from SEM images on high concentration membranes. 20
Figure 29: (a) Comparison of membrane XRD for PNW-6 membrane (LC) to the simulated pattern, (b) and (c) top views of the synthesized PNW-6 membrane. 21
Figure 30: Membrane XRD patterns of PNW-6 membranes synthesized with different times. 22
Figure 31: Top view low magnification SEM images of PNW-6 membranes synthesized as a function of time: (a) 12 hours; (b) 24 hours; (c) 48 hours; (d) 72 hours; (e) 96 hours. 23
Figure 32: Top view high magnification SEM images of PNW-6 membranes synthesized as a function of time: (a) bare support; (b) 12 hours; (c) 24 hours; (d) 48 hours; (e) 72 hours; (f) 96 hours. 24
Figure 33: Cross sectional view SEM images of PNW-6 membranes synthesized as a function of time: (a) bare support; (b) 12 hours; (c) 24 hours; (d) 48 hours; (e) 72 hours; (f) 96 hours. 25
Figure 34: Top view EDS on 48(1) membrane. 26
Figure 35: Cross-sectional view EDS on 48(1) membrane. 26
Figure 36: Schematic of membrane testing module. 27
Figure 37: Modified schematic of membrane testing module. 28
Figure 38: Calibration curves for Xe (a), Kr (b) and Ar (c). 28
Figure 39: Single gas permeances and ideal selectivities on PNW-24 membranes. 30
Figure 40. Single gas permeances and ideal selectivities on PNW-6 (HC) membranes (left) and PNW-6 (LC) membrane (right). 32
Figure 41: 24-hour PNW-6: Xe, Kr concentrations with respect to membrane area 38
Figure 42: 24-hour PNW-6: recoveries and flow ratios with respect to membrane area 39
Figure 43: 48-hour PNW-6: Xe, Kr concentrations with respect to membrane area 40
Figure 44: 48-hour PNW-6: recoveries and flow ratios with respect to membrane area 41
Figure 45: 72-hour PNW-6: Xe, Kr concentrations with respect to membrane area 42
Figure 46: 72-hour PNW-6: recoveries and flow ratios with respect to membrane area 43
Figure 47: 96-hour PNW-6: Xe, Kr concentrations with respect to membrane area 44
Figure 48: 96-hour PNW-6: recoveries and flow ratios with respect to membrane area 45
Figure 49: Difference between Xe permeate recovery and permeate to feed ratio 46

Tables

Table 1: Knudsen diffusion selectivities 29
Table 2: Separation performance of PNW-24 membranes 30
Table 3: Binary gas mixture separation performance of PNW-24 membranes 31
Table 4: Separation performance of PNW-6 (LC) membranes: binary gases. 32
Table 5: Separation performance of membranes under dilute gas conditions 33
Table 6: Separation performance for PNW-6 membranes under dilute gas conditions 34
Table 7: Simulation Parameters 36
Table 8: Permeance Data (mol/m^2/s/Pa) 36
Table 9: Operating Cost Estimate 47

1.0 Introduction

The separation and purification of chemicals constitutes a substantial portion of U.S. energy consumption, accounting for roughly 50% within industry and as much as 15% of the national total. Many of these industrial separation processes are thermally driven, including distillation, evaporation, and drying, all of which have high energy requirements (National Academies of Sciences and Medicine 2019) (Figure 1). To mitigate these energy demands, alternative methods such as pressure-driven absorption have been introduced. Although they significantly reduce the energy consumption, they possess alternate drawbacks. Most absorption processes are impacted by slow flow rates that elongate the separation time, high pressure differentials that complicate equipment design and operation, bulkiness of separation beds, and significant consumption of sorbent material. Such considerations are especially critical in nuclear reactor off-gas processing to carry out tasks such as Kr/Xe separation. Efficiency, safety, and equipment size are critical concerns that must be addressed before the technology can be adapted for various innovative applications.

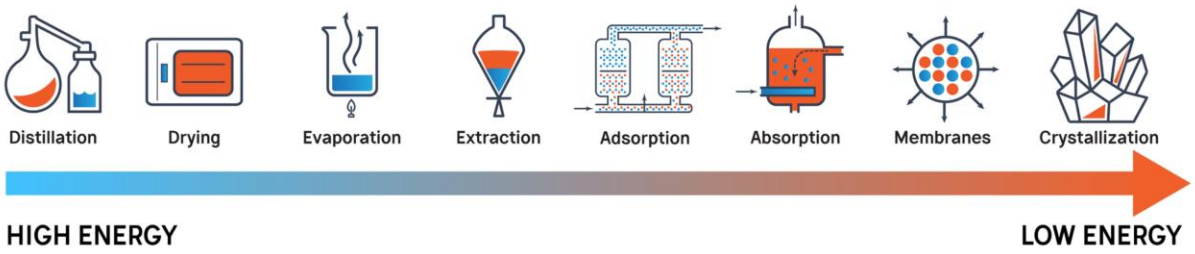

Figure 1. Energy consumption comparison for different separation methods.

To overcome these challenges, membrane-based separation technology is a promising solution because of its improved energy efficiency and less demanding operation conditions (Bernardo, Drioli, and Golemme 2009). Additionally, membrane-based separation is also a versatile platform that could utilize most classes of porous materials toward generating a chemically or physically selective layer. By developing a substrate-supported membrane with uniform microporosity and high radiation tolerance, gas radioisotope separations in nuclear reactor off-gases can feasibly be achieved. Certain crystalline MOFs, zeolites, and porous organic cage compounds have been studied and proven to be effective as the separating layer in adsorption technologies for gas phase Kr/Xe separations (Lucero and Carreon 2020). Unfortunately, these materials have not been directly applied to membrane separation, as multiple design and operating factors must be addressed to optimize the membrane for separation (Gan et al. 2023) (Figure 2). Factors such as membrane thickness, area available for interaction alongside external parameters such as trans-membrane pressure, test temperature play in influential role in separation performance.

Figure 2. Factors contributing to membrane-based separations.

To further the development of a highly efficient and compact Kr/Xe separation bed for off-gas processing equipment, PNNL has previously demonstrated the successful fabrication of various porous MOFs including Hong Kong University of Science and Technology-1 (HKUST-1), onto various porous substrates such as nickel foam and sintered α-alumina support. This prior experience is immensely valuable in the fabrication of tailored membranes for Xe and Kr separation, which are generally achieved by growing or coating materials on suitable supports. This approach allows the thickness, defect degree, and morphology of the porous material layer to be manipulated, all of which influence the overall membrane performance. Additionally, optimizing parameters like flow rate, operating pressure, and temperature is essential when applying these membranes for gas separation under specific concentration conditions. Therefore, our efforts are directed towards optimizing growth conditions, determining the best operational parameters, and assessing radiation tolerance to enhance membrane performance. This comprehensive evaluation aims to assess the potential of these membranes for a wide range of applications. Several Kr/Xe selective materials have been down-selected from previous studies to carry out the membrane separation of Kr from Xe, including organic-inorganic PNW-24 and PNW-6 hybrid materials, a fully organic cage CC3 (composed of 1,3,5-triformylbenzene and (R,R)-1,2-diaminocyclohexane), and zeolitic framework silicoaluminophosphate (SAPO) materials as shown in Figure 3.

2.0 Identify radiation-tolerant materials

As previously reported in the literature (Banerjee et al. 2016), PNW-24 has demonstrated outstanding Kr/Xe separation performance through a combination of molecular simulations and experimental findings, exhibiting exceptional Kr/Xe selectivity even under dynamic flow conditions. These properties position PNW-24 as a promising material for Kr/Xe separation, offering a potential solution over cryogenic distillation with significantly reduced energy requirements. The impressive Xe selectivity of PNW-24 can be attributed to its pore size tailored for Xe molecules, and its densely packed atomic walls that construct a binding site with a strong affinity for Xe molecules (Figure 3a). This property, along with excellent Kr/Xe selectivity and thermal/chemical stability, establishes PNW-24 as a strong candidate for achieving our objective.

CC3 is also a well-known material for the separation of Xe from Kr (Chen et al. 2014). Crystalline CC3 structure features a 3D internal cavity with a size of 4.4 Å, closely resembling the diameter of Xe molecule, which measures 4.1 Å (Figure 3b). Despite the narrowest point in the pore channel having a crystallographic diameter of 3.6 Å, which should hinder diffusion of Xe, the vibrational motion of atoms within the cage molecules is sufficient to permit the passage of Xe molecules. The pore structure of CC3 exhibits an optimal pore size for Kr/Xe separation, as indicated by computational and experimental investigations. Importantly, it lacks smaller interstitial cavities that could competitively adsorb smaller molecules in mixtures, that is, the Kr molecule. CC3 approaches saturation at 1 bar due to its strong affinity for Xe molecules and its appropriate pore dimensions; in contrast, the smaller Kr molecules experience lower uptake and remain much further from saturation at 1 bar. Thus, CC3 is deemed a formidable candidate for accomplishing our objective.

Due to their chemical and thermal stability, ability for molecular sieving and ordered microporous crystalline structure, SAPOs are frequently investigated as materials for gas separation and adsorption applications (Denayer et al. 2008) (Liu et al. 2008; Cheung et al. 2012). SAPO-34 is a silicoaluminophosphate zeolite with a pore size of 3.8 Å that corresponds to CHA topology (Figure 3d). SAPO-34 membranes have been explored for the separation of Xe from air (Wu et al. 2019) and for the separation of gas mixtures containing CO_2, H_2 and CH_4 (Carreon et al. 2008; Poshusta et al. 1998) with a well-studied synthesis procedure. SAPO-56 is a small pore silica aluminaphosphate where the phosphorous and aluminum atoms are substituted by silicon atoms. SAPO-56 has a confined pore size of 3.4 x 3.6 Å and corresponds to AFX topology (Wilson et al. 1999). Since the separation of Xe and Kr could be governed by both diffusion (since Kr's diffusion is higher) and adsorption (Xe having higher adsorption), there is an additional value to choose a material that has a pore size lying between the kinetic diameters of Xe and Kr, facilitating molecular sieving as a competing factor to the other two separation phenomenon.

A subclass of MOFs exhibit ordered porous structure and a hybrid framework with metal clusters and imidazole ligands. In particular, PNW-6 possesses an open-framework structure. Appealing properties such as flexibility of frameworks (Hayashi et al. 2007; Li and Kim 2012), high specific surface area and chemical and thermal stability of 500°C (Liu, Liu, and Huang 2020) makes PNW-6 an excellent choice of material to be explored for gas separations. The pore size of PNW-6 (shown in Figure 3c) is ≅ 3.2 Å.

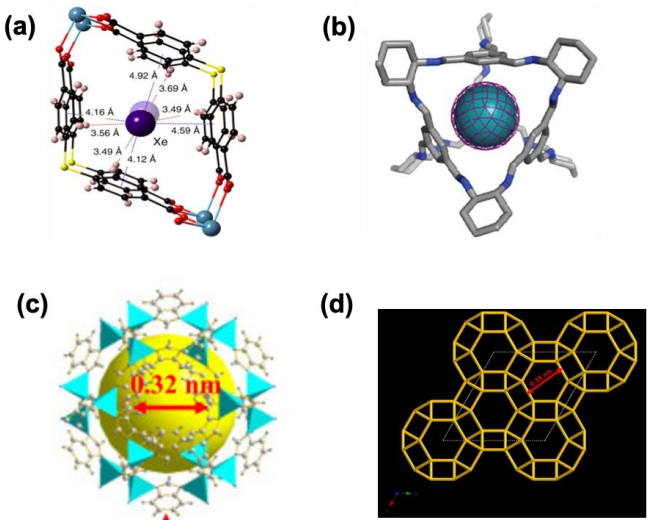

Figure 3. (a) Xe molecule position in PNW-24 cavity determined by single-crystal X-ray diffraction; (b) the size to accommodate a single Xe molecule in CC3 cavity; (c) pore size and sodalite topology of PNW-6; (d) CHA topology of SAPO-34 (Chen et al. 2014; Banerjee et al. 2016).

3.0 Powder synthesis and characterization of materials

Miniflex II (Rigaku Co., Japan) was used to collect PXRD patterns of the powder samples in the range of angles between 5 and 40 degrees with Cu-Kα radiation and a wavelength of 1.5Å. SEM images of the powders and the top and cross-sectional images of the membranes were collected with a JEOL JSM-7001F field emission SEM (JEOL, Japan) with an accelerating voltage of 5kV. The samples were activated overnight (~16hours) before collecting Brunner-Emmett-Teller (BET) surface area as well as room temperature Xe and Kr isotherms with the help of a 3Flex instrument (Micromeritics Instruments, USA). Particularly for the room temperature isotherms (298K), the temperature of the bath was maintained with an ethylene glycol circulation system.

3.1 PNW-24

We synthesized radiation-tolerant PNW-24 powders according to the synthesis procedure reported in the literature (Tozawa et al. 2009; Banerjee et al. 2016). As obtained off-white powder was washed three times with fresh EtOH and dried at 60 °C in a vacuum oven overnight to remove any solvent. The PXRD patterns of the synthesized PNW-24 powders matched well with the simulated pattern, indicating successful synthesis of the material as shown in Figure 4.

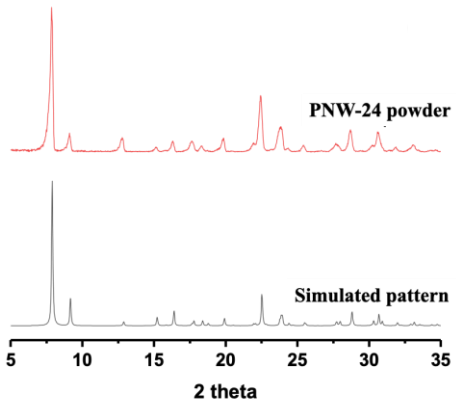

Figure 4: Comparison of Xray diffraction patterns of synthesized PNW-24 powders with simulated pattern.

SEM images of the synthesized PNW-24 powders attest to the expected morphology of PNW-24 powders and is shown in Figure 5 (a and b).

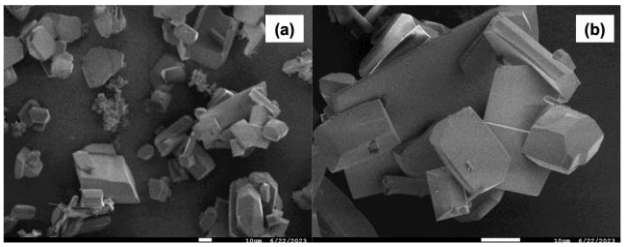

Figure 5: SEM images of PNW-24 powders.

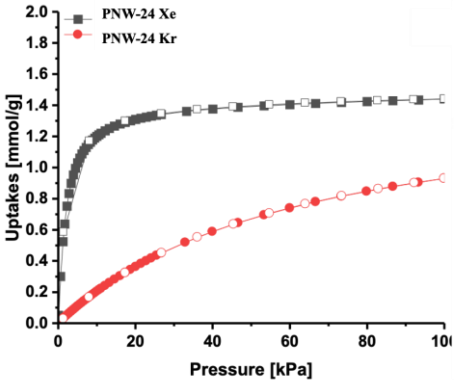

Figure 6: Xe and Kr uptake on PNW-24 powders

The Xe and Kr adsorption isotherms of PNW-24 particles were measured at 298K and 1 bar (Figure 6), given the structural confirmation of its successful synthesis. PNW-24 exhibits exceptional Xe and Kr selectivity, with particularly high Xe adsorption uptake at low pressure. This is highly advantageous for selective Xe separation, which often exists in very low concentration (i.e., partial pressures) in off-gases.

3.2 PNW-6

PNW-6 powders were synthesized with a solvothermal approach using a Teflon-lined stainless steel Parr reactor. After natural cooling, the Teflon liner was carefully removed, and the synthesized PNW-6 powders were separated using centrifugation. The powders were then stored at 70°C for 24 hours before PXRD patterns were collected, as presented in Figure 7. It was observed that most of the characteristic peaks from the simulated patterns matched well with the synthesized powders.

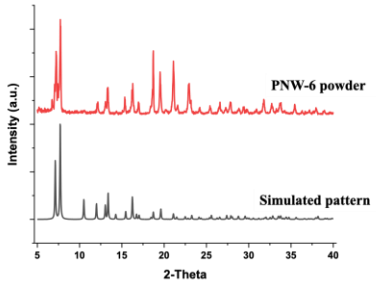

Figure 7: Comparison of PXRD patterns of synthesized PNW-6 crystals to the simulated pattern.

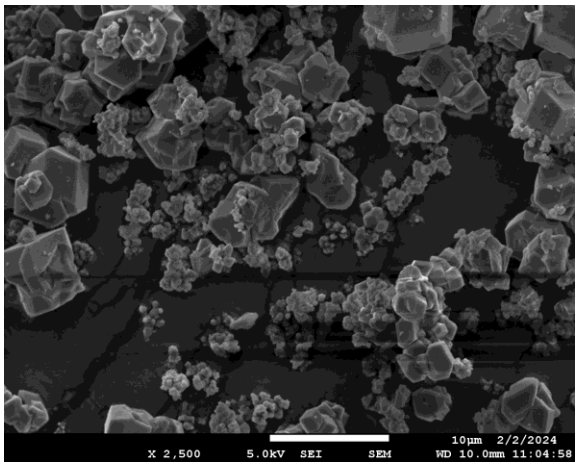

Figure 8: SEM image of synthesized PNW-6 crystals.

The SEM images of the as-synthesized PNW-6 crystals are shown in Figure 8 and they confirm the morphology of PNW-6. Xe, Kr and Ar isotherms at 298K was collected on the PNW-6 powders (Figure 9Figure 9a) after activating them at 150°C for 16 hours. Upon analysis, a maximum Xe uptake of around 2.25 mmol/g was observed at 1bar. The uptake capacity of Ar and Kr were considerably low at 1bar. Further, at about 0.5 bar, there is a steep uptake of Xe in comparison to Kr and Ar (Figure 9b), which could be indicative of a sorbate-induced gate opening or swinging effect that has been observed in PNW-6 previously (Noguera-Díaz et al. 2016). Upon closer examination of the lower pressure regions (Figure 9b) pertaining to lower concentrations of each analysis gas, there is a difference between quantities of Xe, Kr and Ar uptake. This difference, along with the gate opening effect, indicates viability of PNW-6 to be used as a material for the separation of gases.

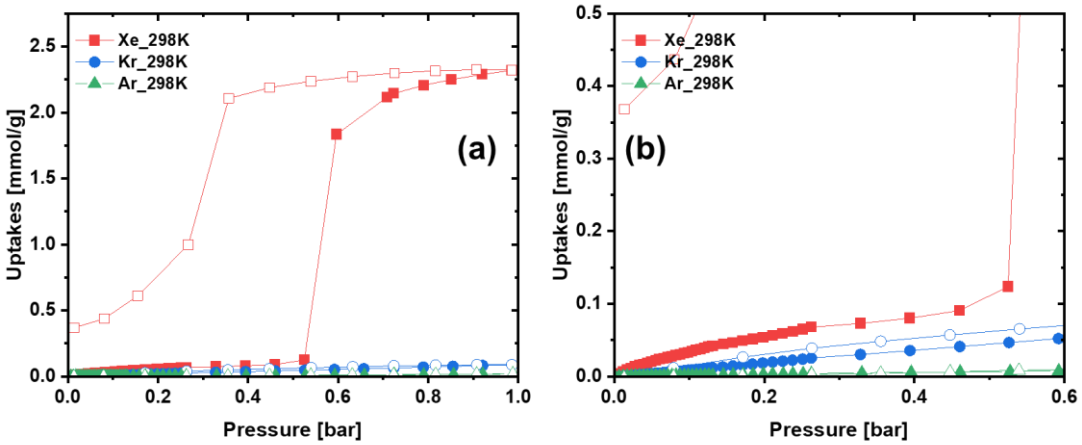

Figure 9: (a) Room temperature uptake of Ar, Kr and Xe on PNW-6 crystals and (b) focused isotherm on the low-pressure range.

3.3 CC3

CC3 crystals were synthesized using two synthesis procedures: for solvothermal synthesis, 1g of TFB was added to 15mL DCM and stirred for 5 minutes. Another solution was made by mixing 1.14g of DCH and 15mL DCM. Both the solutions were then mixed slowly and

left to react solvothermally at 50°C for 48 hours in a Teflon-lined stainless steel Parr reactor. After cooling down naturally to room temperature, CC3 powders were harvested by centrifuging and cleaning with 95:5 EtOH: DCM thrice and dried in a vacuum oven for 24 hours at 65°C. To synthesize CC3 powders at room temperature, 81mg of TFB was added to 3mL of DCM to form solution 1. Solution 2 was prepared by adding 85mg of DCH and 3mL DCM. Solutions 1 and 2 were mixed slowly and left to react at room temperature. After 48 hours, solvent was decanted and fresh DCM (3mL) was added to redisperse the material, which was then filtered through a 110 mm Whatman filter paper to obtain CC3 powders. PXRD patterns of the powder samples were collected and is shown in Figure 10. Most of the characteristic peaks of the synthesized powders match with the simulated pattern indicating successful synthesis of CC3.

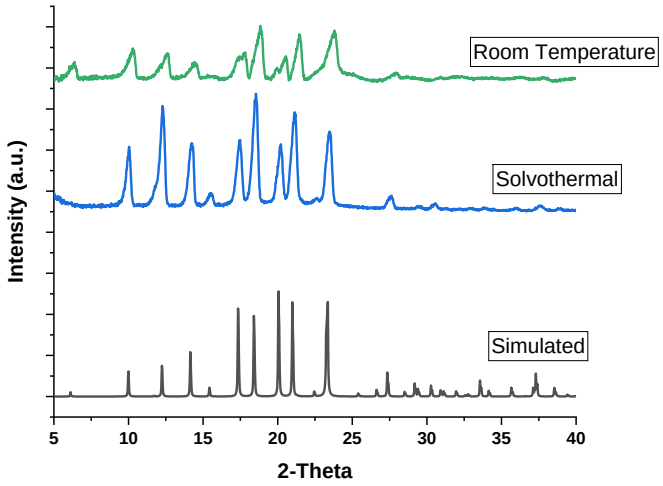

Figure 10: PXRD pattern comparison of CC3 powders synthesized using solvothermal approach and room temperature approach.

SEM images were collected to confirm the morphology of synthesized CC3 powders. As shown in Figure 11a-b, CC3 possesses an octahedral shape with particle size of 5–10 μm.

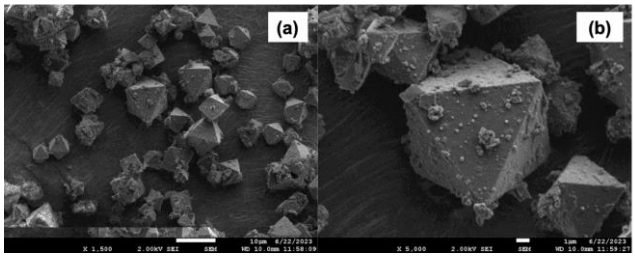

Figure 11: SEM images of CC3 powders.

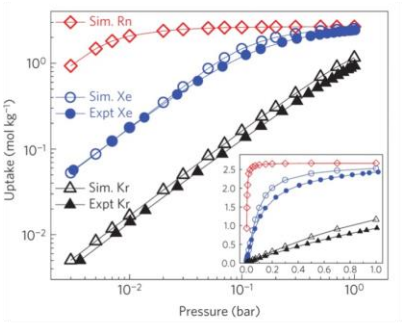

Figure 12. The Xe and Kr uptakes at 298 K of CC3 from literature (Chen et al. 2014).

The Xe and Kr adsorption isotherms of CC3 were obtained from literature (Figure 12). CC3 exhibits high Xe uptake in comparison to Kr as well as a higher Xe uptake at lower pressures indicative of lower concentrations.

3.4 SAPO-56

SAPO-56 crystals were synthesized per the procedure reported in the literature (Wu et al. 2017) and the ratios used were 2.0 TMDH:0.6 SiO_2:0.8 Al_2O_3:1.0 P_2O_5:40 H_2O. Aluminum isopropoxide was used as the alumina source, Ludox-40 silica as the silica source, phosphoric acid as the source for P_2O_5, and TMHD was *N*,*N*,*N*′,*N*′-tetra-methyl-hexane-1,6-diamine. The alumina source was added to deionized (DI) water and stirred at 500 rpm for 1 hour at room temperature. Phosphoric acid was then added to the mixture and stirred for 1 more hour. Then, the silica source was added to the mixture and let stir for 2 hours. Finally, TMDH was added, and the mixture was allowed to stir overnight at the same speed at room temperature. After we observed a homogeneous solution (Wu et al. 2017), it was transferred to a Teflon-lined stainless steel Parr reactor and left to react at 200°C for 24 hours. After cooling naturally to room temperature, the supernatant was collected and centrifuged at 3000 rpm for 10 minutes, followed by cleaning with DI water thrice using the same centrifuging conditions. The powders obtained were then dried overnight in the vacuum oven at 100°C. Then they were transferred to a ceramic crucible to be calcined at 550°C for 10 hours at a heating and cooling rate of 2°C/min and 5°C/min, respectively. PXRD patterns of the SAPO-56 powders were collected and is presented in Figure 13. There is a reasonable agreement of the synthesized material with the simulated pattern. Appearance of additional peaks could be associated to the presence of organic template that was used in synthesizing SAPO-56 powders.

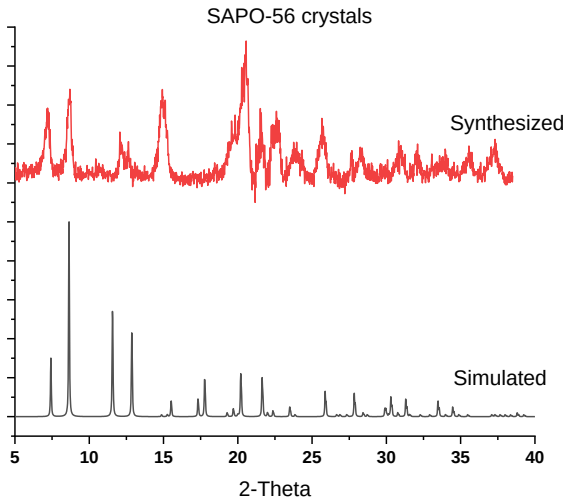

Figure 13: PXRD pattern comparison of SAPO-56 seeds.

3.5 SAPO-34

We relied on literature (as shown in Figure 14) for the Xe and Kr isotherms on SAPO-34. At lower operating pressures (corresponding to lower concentrations of Xe and Kr), there is a less significant difference between the gas uptake capacity of Xe and Kr due to higher dipole polarizability of Xe in comparison with Kr. Figure 14 also shows the steep uptake of Xe and Kr as the temperature is reduced. Breakthrough experiments also revealed higher diffusivity of Kr over Xe, indicating that all separation phenomenon (molecular sieving, adsorption and diffusion) could be simultaneously contributing to the separation.

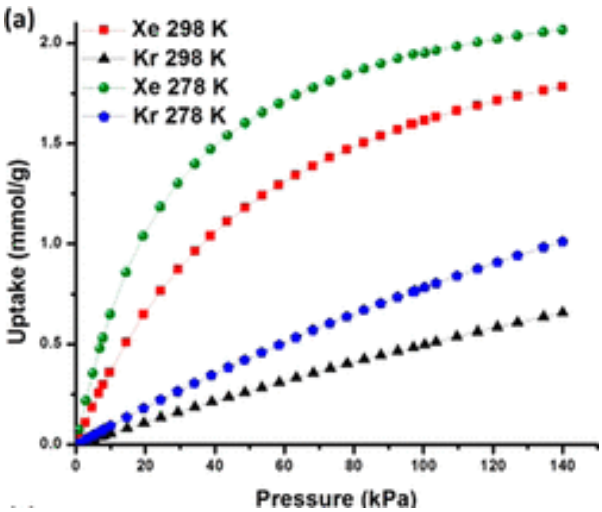

Figure 14: Xe and Kr isotherms on the SAPO-34 zeolites, adapted from (Feng, Zong et al. 2016)

SAPO-34 crystals were synthesized using three different ratios of the precursors. For all the syntheses, aluminum isopropoxide was used as the alumina source, Ludox-40 silica as the silica source, phosphoric acid as the source for P_2O_5, tetraethylammonium hydroxide (TEAOH; 35wt% aqueous solution) was the organic template, and DPA was dipropyl amine. For synthesis 1, $1Al_2O_3$: 1H3PO4: 0. 3SiO2:1TEAOH:1. 6DPA:77sH2O ratio was used. The aluminum source, H_3PO_4, and DI water was added to a beaker and stirred at 500 rpm for 2 hours. Ludox silica was added to the mixture and let stir for 2 more hours. Finally, TEAOH and DPA were added, and the gel was allowed to age for 3 days at 50°C. After obtaining a homogeneous mixture, the gel was transferred to a Teflon-lined reactor and left to react at 220°C for 24 hours. After natural cooling to room temperature, the supernatant was centrifuged at 4000 rpm for 20 minutes followed by washing with DI water 3 times. The powder obtained was then stored at 100°C oven for 24 hours after which it was calcined at 550°C for 5 hours with a heating and cooling rate of 1°C/min and 10°C/min respectively.

For synthesis 2, $1Al_2O_3$:$2P_2O_5$:0.6 SiO_2:4TEAOH:150 H_2O ratio was used. The aluminum source and DI water were added to a beaker and stirred at 500 rpm for 1 hour. Then H_3PO_4 was added and stirred for 2 hours. Ludox silica was then added to the mixture and stirred for 3 more hours. Finally, TEAOH was added, and the gel was allowed to age for 4 days at 50°C. After obtaining a homogeneous mixture, the gel was transferred to a Teflon-lined reactor and let react at 220°C for 24 hours. After natural cooling to room temperature, the supernatant was centrifuged at 3300 rpm for 10 minutes, followed by washing with DI water three times. The powder obtained was then stored in a 100°C oven for 24 hours, after which it was calcined at 400°C for 4 hours with a heating and cooling rate of 0.8°C/min.

For synthesis 3, 1 Al_2O_3:$1P_2O_5$:0.3 SiO_2:1TEAOH:1.6 DPA: 300 H_2O ratio was used. The aluminum source and DI water were added in a beaker and stirred at 500 rpm for 1 hour. Then H_3PO_4 was added and stirred for 2 hours. Ludox silica was then added to the mixture and stirred for 3 more hours. Finally, TEAOH and DPA was added, and the gel was allowed to age for 4 days at 50°C. After obtaining a homogeneous mixture, the gel was transferred to a Teflon-lined reactor and maintained a reaction at 220°C for 24 hours. After natural cooling to room temperature, the supernatant was centrifuged at 3300 rpm for 10 minutes followed by washing with DI water 3 times. The powder obtained was then stored at 100°C oven for 24 hours, after which it was calcined at 400°C for 4 hours with a heating and cooling rate of 0.8°C/min. The PXRD patterns of the synthesized SAPO-34 were then compared to the simulated pattern. Many of the prominent peaks match with the simulated pattern, as shown in Figure 15, indicating successful synthesis of SAPO-34 crystals.

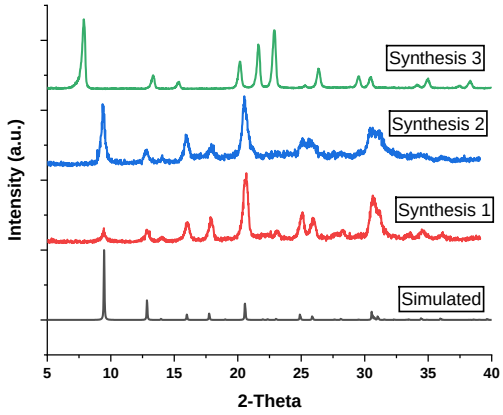

Figure 15: PXRD patterns of SAPO-34 powders synthesized using different ratios of precursors in comparison to simulated pattern.

4.0 Fabrication of membranes on porous support

Membranes are typically prepared on porous supports to impart necessary mechanical strength and mitigate the inherent powder-like properties. While various supports have been used for depositing/growing continuous films, we focused on porous alumina supports in this work. We purchased the porous alumina supports with 1-inch diameter from McMaster Carr as rods. The rods were then cut to 1.8 mm thickness discs to be accommodated into our membrane permeation testing module. The porous alumina supports were then cleaned with deionized water at 100ºC for 2 hours and dried in a vacuum oven at 150ºC for 24 hours. Further cleaning of the porous discs was done with ethanol. The cleaned supports were then stored for future experiments. Any visually defective (cracks or greased supports) were discarded.

4.1 Fabrication of PNW-24 membrane by seeding method

Seeded PNW-24 membrane was fabricated as illustrated in Figure 16. The membrane solution was placed in a 100 ºC oven for about 5 min, inducing the gel-like mixed solution to become a completely clear solution. This process is critical for the homogeneous introduction of the precursor solution to the support. To this clear solution, a hot (140 ºC) polished alumina support was added. Immediately, small bubbles would emanate from the surface of the support, indicating uptake of the solution into the pores of the alumina support. After the support had soaked in the concentrated precursors solution for about 5 minutes, it was removed and placed in a preheated 180ºC oven for 15 min, forcing the precipitation of materials.

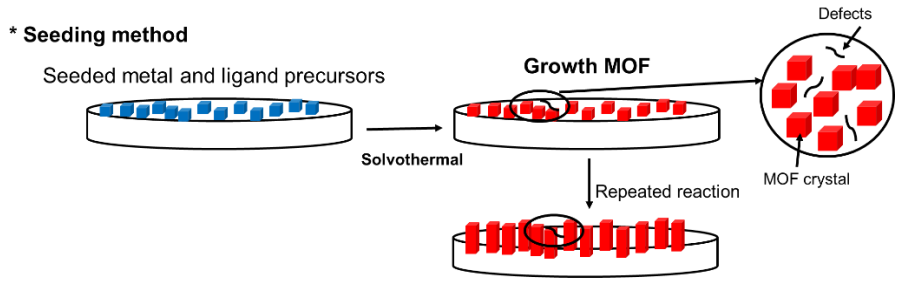

Figure 16: Schematic of seeding approach adapted for PNW-24 membranes.

The seeded support was then used in a solvothermal synthesis for the synthesis of PNW-24 membrane. The fabricated membrane was then washed with fresh acetone and soaked in excess acetone for 1 day. After the membrane was dried at room temperature overnight under vacuum, the crystal phases were investigated through PXRD measurements and are shown in Figure 17a and Figure 18. To increase the membrane thickness, the synthesis procedure was repeated multiple times (indicated by 3R, 4R, and 5R, where R stands for repetitions in synthesis) with each membrane sample.

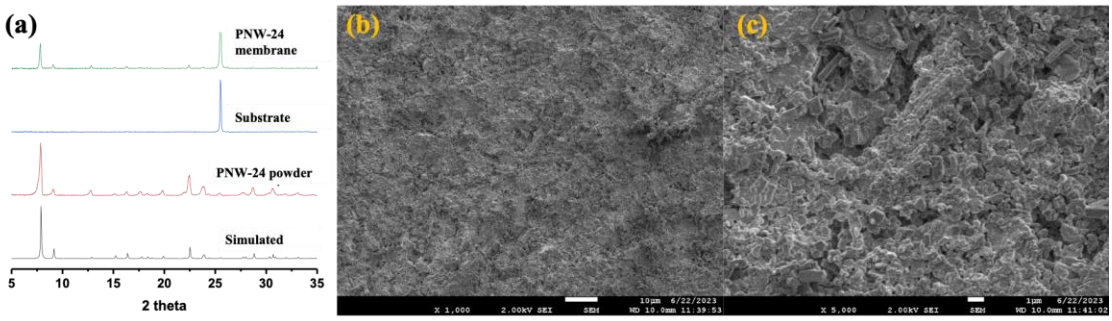

Figure 17: The PXRD pattern of fabricated PNW-24 membrane with (a) simulated crystallography structure; the SEM images of PNW-24 membrane at magnifications (b) 1000X and (c) 5000X, respectively.

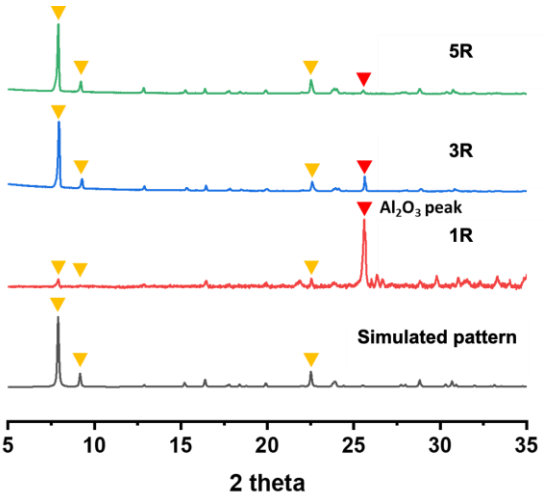

Figure 18: Membrane XRD pattern of PNW-24 membrane with different layers.

SEM images of the top view and cross-sectional view of the synthesized PNW-24 membranes were collected and are shown in Figure 19. From the top views (Figure 19 [a, c, e]), as the number of layers deposited increased; the crystal morphology remained the same, but the size of the crystals increased. There are also noticeable smaller crystals observed both in Figure 19 (c) and (e), indicating an effect of both nucleation and growth occurring simultaneously at the support interface.

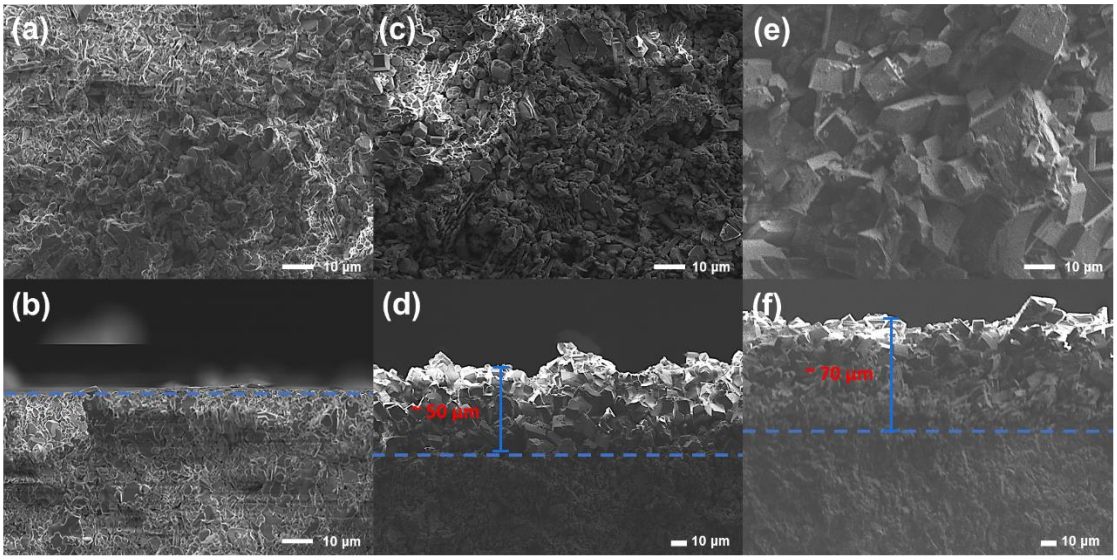

Figure 19: Top views (a, c, e) and cross-sectional views (b, d, f) of PNW-24 membranes synthesized using seeding approach; 3R (a, b), 4R (c, d) and 5R (e, f).

4.2 Fabrication of PNW-24 membrane by surface functionalization

A schematic of the surface modified synthesis of PNW-24 membrane is shown in Figure 20.

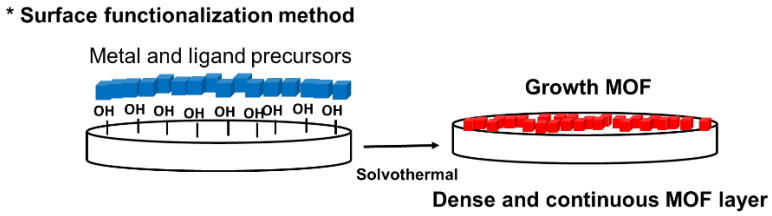

Figure 20: Schematic of surface functionalization approach adapted for PNW-24 membranes.

The fabricated PNW-24 membrane was washed with fresh EtOH and soaked in EtOH for 1 day. It was dried in a vacuum oven at 60ºC overnight. XRD patterns were then collected on the PNW-24 membranes and is shown in Figure 21 (a). Comparison of the XRD pattern of the synthesized membrane to the seeded PNW-24 membrane indicated increased intensity of PNW-24 peaks indicative of membrane formation on the substrate. Top view SEM images collected on the membrane also confirms the morphology of PNW-24 crystals as shown in Figure 21 (b) and (c).

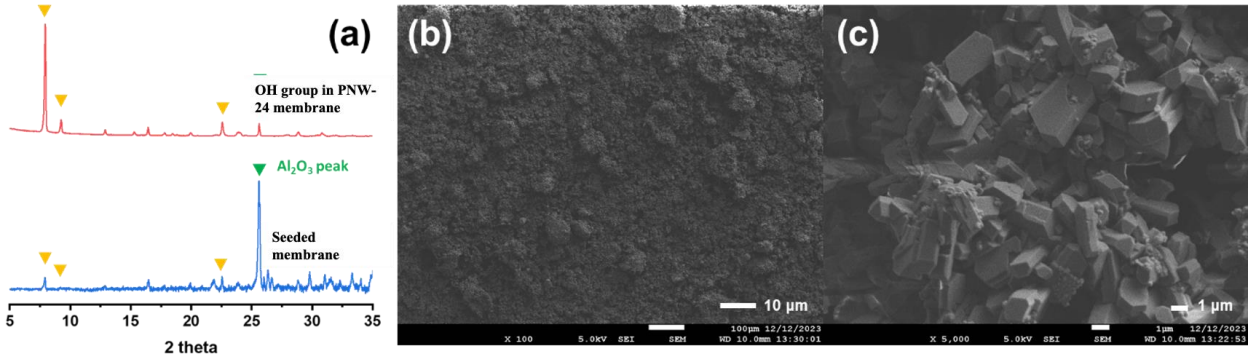

Figure 21: (a) Comparison of seeded PNW-24 membrane to functionalized PNW-24 membrane, (b) and (c) top view of crystals deposited on PNW-24 membrane.

4.3 Fabrication of CC3 membrane

Several methods were explored to synthesize continuous CC3 membranes. For in-situ growth, 0.3g of TFB was added to 40mL DCM and sonicated for 10 minutes. Another solution was prepared by adding 0.3 g of DCH to 40 mL DCM followed by 40 mL of TFA. The bare alumina support was wrapped on one side with Teflon tape and heated overnight in an oven at 65°C. The two solutions were mixed, and the hot Teflon-wrapped support was immersed in the mixture. This setup was left undisturbed for 48 hours at room temperature, after which the support was removed and rinsed with EtOH to remove any unreacted precursors. The support was then stored at 70°C in a vacuum oven prior to collecting XRD pattern, as shown in Figure 22. It can be observed that with one layer of in-situ CC3 membrane growth at room temperature, the intensity of alumina peak is high, indicating lower coverage on the support.

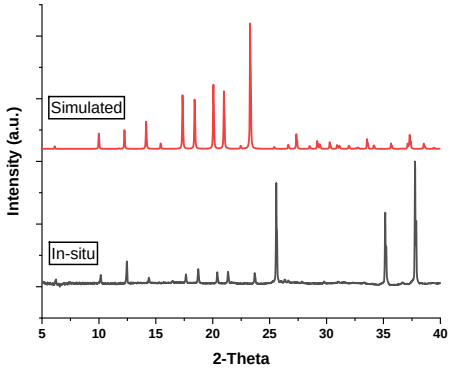

Figure 22: CC3 in-situ room temperature membrane XRD compared with simulated pattern.

A drop-casting method was employed by dispersing 40 mg of the seeds synthesized using solvothermal technique in 20mL DCM. This solution was then slowly dropped on the hot Teflon-wrapped support (70°C) using a pipette. Then the support was moved back to the oven for solvent evaporation. These steps were repeated seven times, and the support was allowed to dry for 24 hours at 70°C in the vacuum oven. We observed a thick layer of CC3 powders deposited on the substrate and the XRD pattern of the membrane in comparison to the simulated pattern, as shown in Figure 23. Although a thick layer of CC3 (as yellow color precipitates) could be visually observed on the support the intensity of alumina peak is still high, indicating

medium to low growth on the support. The in-situ growth and drop-casting are techniques used to deposit a thin film layer unlike binding or intergrowing the material in the substrate. While these methods are relatively simple, they could result in membrane delamination or peel off.

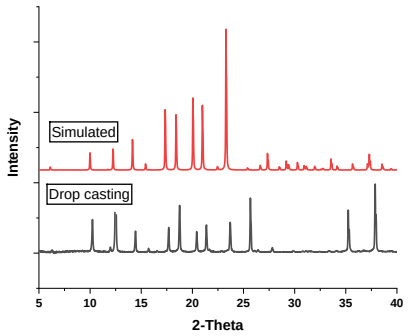

Figure 23: CC3 drop-casted membrane XRD compared with simulated pattern.

For solvothermal synthesis, 70 mg of the powders obtained with room temperature synthesis were dispersed in 20 mL DCM. Hot Teflon-wrapped support was soaked in the seed solution for 1 hour, after which the support was removed and placed in the vacuum oven at 70°C for an hour for solvent evaporation, repeating the steps twice. Two solutions were prepared, the first with 103 mg of TFB+ 15 mL of TFA, and the second with 20 mL DCM and 103 mg DCM + 20mL DCM. Each solution was prepared separately and carefully added together to the Teflon-lined Parr reactor. A Teflon-wrapped support stored in vacuum oven at 70°C was then carefully placed horizontally, making sure the support was completely immersed in the combined membrane solution. The reaction was maintained at 50°C for 48 hours, after which it was naturally cooled. The support was removed from the reactant mixture and rinsed with EtOH to remove any unreacted precursors. The solvothermal synthesis was repeated to grow a second layer of CC3 on the support. In comparison with the other two synthesis strategies, the amount of CC3 deposited was low as observed from the membrane XRD (Figure 24). Although the characteristics peaks of CC3 were identified from the membrane XRD, the intensity of alumina peaks were considerably high, indicating lesser coverage and lower amounts of CC3 grown. To increase the thickness of deposited layers, the solvothermal synthesis procedure needs to be repeated multiple times.

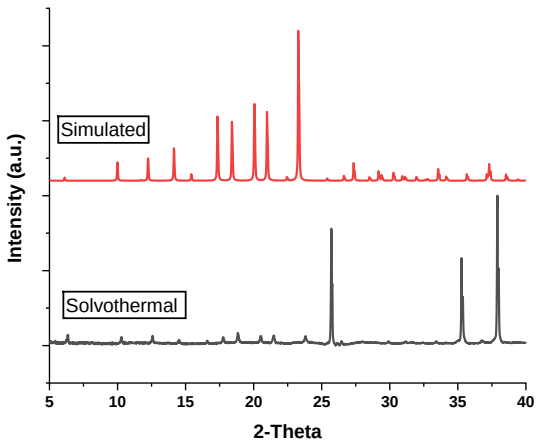

Figure 24: CC3 solvothermal membrane XRD compared with simulated pattern.

4.4 Fabrication of SAPO-56 membrane

A 5wt% seed solution was prepared using previously synthesized SAPO-56 seeds and DI water. Hot (80°C) Teflon-wrapped supports were immersed in the seed solution for 10 minutes, then the support was moved to the oven to remove water. This step was repeated twice, and the membrane was left in the vacuum oven at 100°C overnight. SAPO-56 membrane was synthesized by seeding method using a gel concentration calculated with 2.0 TMDH:0.6 SiO_2:0.8 Al_2O_3:1.0 P_2O_5:40 H_2O. The aluminum source and DI water was mixed and stirred at 500 rpm for 1 hour. Then, H_3PO_4 was added, and the mixture was stirred for 1 hour, followed by adding the silica source and stirring the mixture for 2 more hours. Finally, TMDH was added, and the mixture was aged overnight at room temperature. The homogenous membrane gel was then transferred to a Teflon-lined stainless-steel Parr reactor, and the seeded alumina support was then immersed carefully into the Teflon liner. SAPO-56 membranes were synthesized at 210°C for 48 hours. After natural cooling, the membrane was removed, rinsed with DI water, and heated at 100°C in the vacuum oven. The membrane XRD patterns of SAPO-56 did not indicate all characteristic peaks (Figure 25). This might be because calcination was not performed to remove the template that helped with the formation of SAPO-56 material. Thus, addition of further layers by means of solvothermal approach is necessary to facilitate the growth of SAPO-56 crystals on the alumina support.

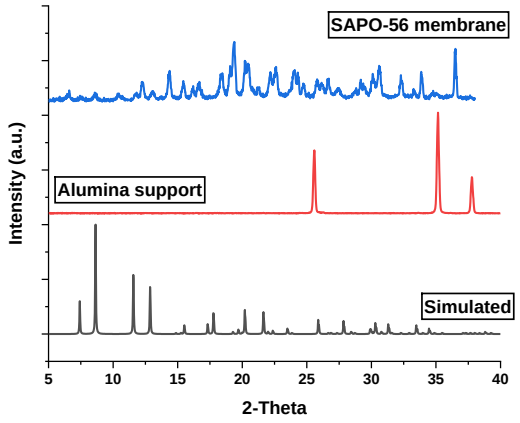

Figure 25: SAPO-56 membrane XRD compared with simulated pattern.

4.5 Fabrication of SAPO-34 membrane

A SAPO-34 membrane was synthesized using an in-situ synthesis procedure with 1 Al_2O_3:1P_2O_5:0.6 SiO_2:1 TEAOH:56 H_2O. The phosphorous source, alumina source, and DI water was added to a beaker and let mix in room temperature for 12 hours. TEAOH and silica source were then added and let stir for another 30 minutes. The gel was aged for 48 hours at room temperature. Hot (80°C) Teflon-wrapped alumina support was then soaked in the membrane gel for 3 hours prior to transferring to the Parr reactor, and then to the oven at 184°C for 20 hours. After naturally cooling to room temperature, the membrane was taken out and rinsed with DI water and dried at 100°C for 24 hours. Typically three or four layers of membrane synthesis are recommended for the SAPO zeolites but in our membrane synthesis, we have only used one layer

to be mindful about the time required for synthesis. Unlike SAPO-56, many characteristic peaks of simulated SAPO-34 were identified from membrane XRD indicating the correct growth (Figure 26). The intensity of alumina peak is also considerably less than that observed for CC3 and SAPO-56 membranes.

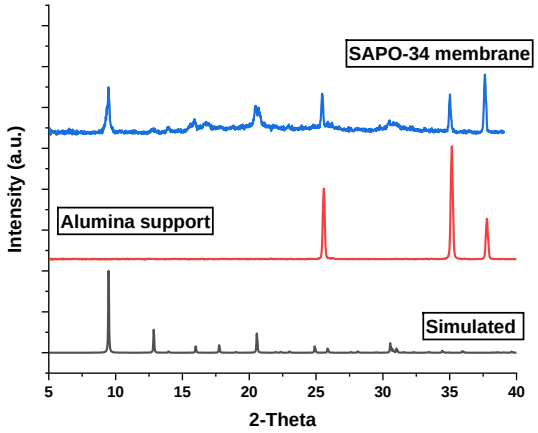

Figure 26: SAPO-34 membrane XRD compared with simulated pattern.

4.6 Fabrication of PNW-6 membrane

It has been reported in the literature (Liu, Liu, and Huang 2020) that due to thermodynamic preference, PNW-6 forms as crystals rather than growing on a substrate. So, chemical modification is an essential step to make the substrate preferential for the nucleation and growth of PNW-6 crystals. While seed coating is a popular strategy for membrane synthesis, it requires an additional step which is time consuming and homogeneous seed distribution is also not guaranteed. We adapted a simple and effective strategy from literature (Liu, Liu, and Huang 2020) for the seeding-free synthesis of PNW-6 membrane by using 3-aminopropyltriethoxysilane (APTES) as covalent linker between the material l and the porous support. By covalent bonds, the PNW-6 nutrients were attracted and attached onto the support surface for the facile growth of continuous PNW-6 membranes. The modification with APTES offers several advantages for practical membrane synthesis. It effectively prevents pore blockage of porous supports and is much simpler compared to the seed coating method. To gain the concentration of hydroxyl groups on the surface of support, the alumina support was first soaked in a saturated NaOH solution for 1 day. Then, the support was washed using fresh water with sonication and dried at 90ºC for 2 hours. The APTES was able to bind to the surface by the silane group and act as a covalent linker for binding PNW-6 crystals.

The PNW-6 membrane with high concentration of precursors was fabricated by following reported literature (Huang et al. 2016). The purple-colored coated product was cleaned with fresh EtOH several times and soaked in the fresh EtOH for 1 day. The membrane was dried in a vacuum oven at 70ºC overnight; the resulting membrane was named PNW-6 membrane (HC).

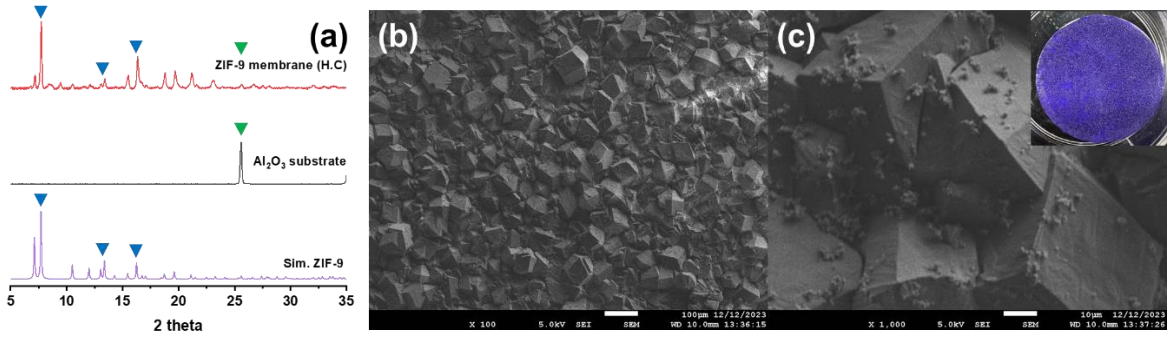

Figure 27: (a) Comparison of membrane XRD for PNW-6 (HC) membrane to the simulated pattern, (b) and (c) top views of the synthesized PNW-6 membrane.

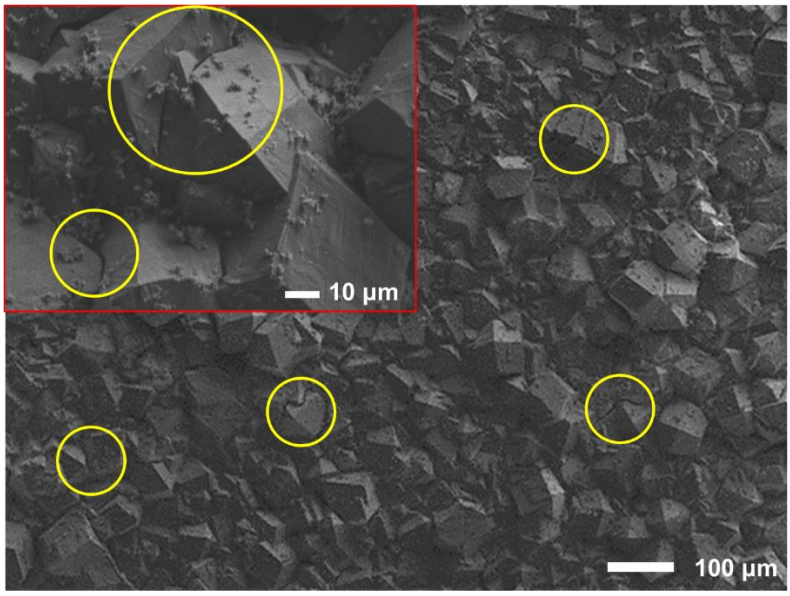

Figure 28: Intercrystallite defects created as seen from SEM images on high concentration membranes.

From the XRD patterns of the HC PNW-6 membranes, there is an excellent match with the simulated patterns. The intensity of alumina peaks also decreased upon membrane synthesis indicating a thick and uniform growth of PNW-6 crystals Figure 27a. Upon analyzing the SEM images as shown in Figure 27 (b) and (c) the size of crystals is about 100 µm. The insert on Figure 27 (c) shows an image of the purple colored PNW-6 coating on the substrate. We then collected a higher magnification image on the HC membrane which revealed intercrystallite defects as shown in Figure 28, circled in yellow indicating spaces/cracks formed between crystals. These defects could act as preferable pathways for gases to flow through rather than interacting with the material leading to poor or wrong separation performance.

The PNW-6 membrane with low concentrated precursors was fabricated with a reduced number of precursors. The obtained membrane was washed with fresh DMF and EtOH and was soaked

in the EtOH for 1 day. The membrane was dried in a vacuum oven at 70 ºC overnight; the resulting membrane was named PNW-6 membrane (LC).

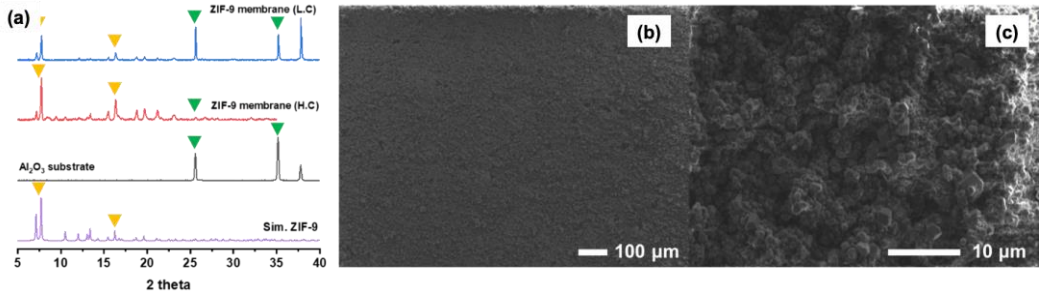

Figure 29: (a) Comparison of membrane XRD for PNW-6 membrane (LC) to the simulated pattern, (b) and (c) top views of the synthesized PNW-6 membrane.

Comparison of XRD pattern of the LC membrane with the HC membrane as well as simulated pattern (Figure 29 (a)) confirmed the synthesis of PNW-6 but with lower thickness as compared to the HC membrane as indicated by the intensity of alumina peak. The SEM images (Figure 29 (b) and (c)) did not reveal any significant defects or cracks as seen in the HC membrane.

4.7 Optimizing reaction time for PNW-6 membrane

We further optimized the PNW-6 membranes synthesis conditions by fabricating PNW-6 (LC) membrane under different synthesis times. During optimization, we maintained the synthesis temperature and concentration of precursors constant to evaluate the effect caused only due to time as a variable. Figure 30 shows the membrane X-ray diffraction pattern for five different membranes synthesized for 12, 24, 48, 72, and 96 hours. As observed, most of the characteristic peaks in the simulated pattern are persistent and prominent for all the membranes synthesized. We could also notice the intensity of the peaks from alumina supports decreasing as the synthesis time increases. Synthesis optimization also plays a crucial role in cost estimation, especially while scaling up the process, as the time required to synthesize one membrane could have a direct effect on the amount of energy input.

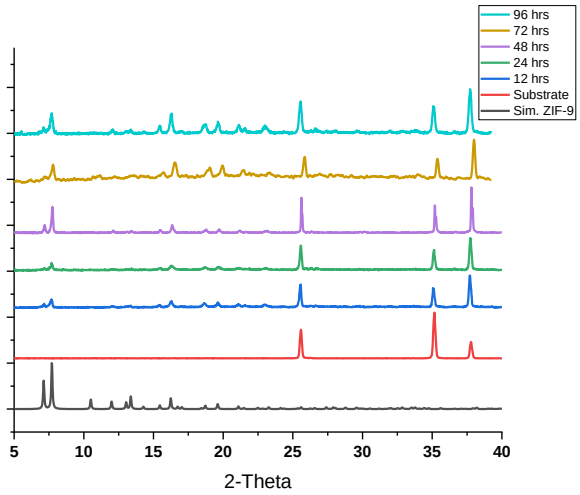

Figure 30: Membrane XRD patterns of PNW-6 membranes synthesized with different times.

Initial assessment of the SEM top view did not indicate any visible cracks or defects on any of the membranes. As seen in Figure 31 (a), the 12-hour membrane indicates isolated island growth of PNW-6 on the top layer indicative of non-uniform growth of the crystals after an initial layer. When left in membrane solution for an additional 12 hours at the same temperature, there is a more uniform growth of PNW-6 crystals. Unlike the 12-hour membrane, we could clearly identify many small size PNW-6 crystals on the 24-hours membrane (Figure 31b). In the case of the 48-hour membrane (Figure 31c), we observed a thicker and closer crystal growth, indicating increased uniformity. There was an increase in crystal size for the 48-hour membrane indicating the growth of the formed membrane layer. The 72-hour membrane (Figure 31d) showed nonconformity in the crystal morphology, but in the 96-hour membrane (Figure 31e), the PNW-6 crystals could be observed. The membranes grown on supports were coated with Iridium prior to collecting SEM images to avoid chargeability issues and to obtain images with better clarity. The density of Iridium is 22.56 c/cm^3. To cover a 1-inch diameter membrane support with 20 Å thickness, 0.0228 µg of Iridium would be necessary. The amount of iridium necessary to cover the membrane was calculated to consider the possible effects due to coating.

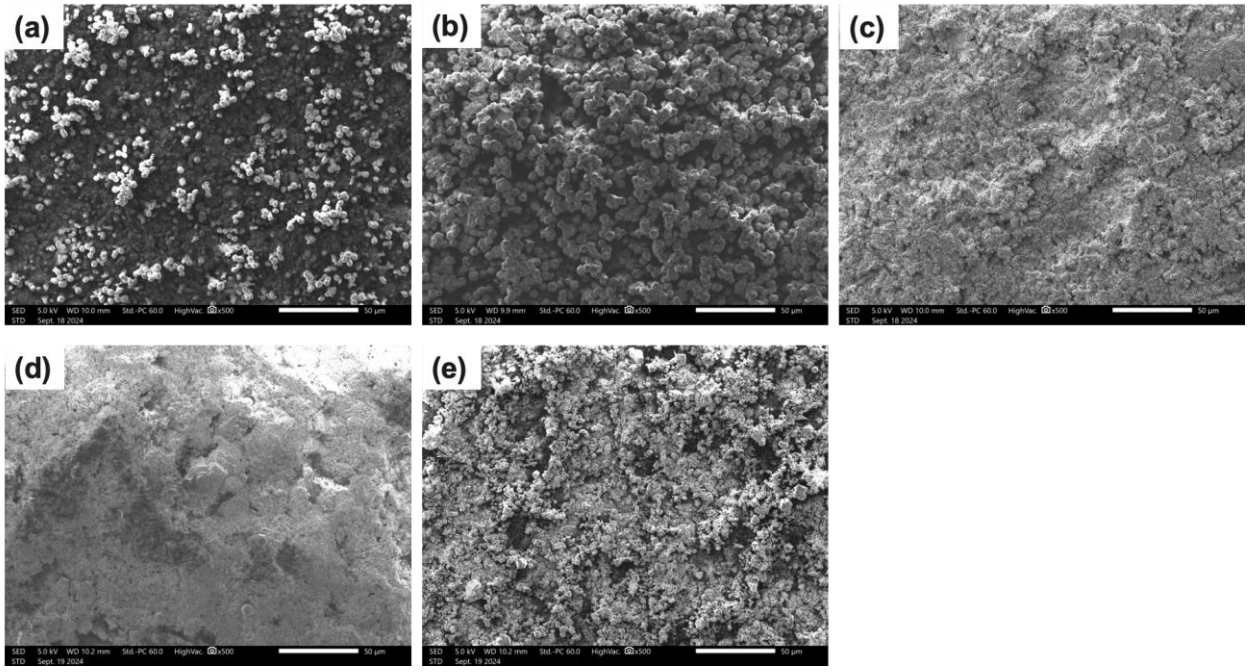

Figure 31: Top view low magnification SEM images of PNW-6 membranes synthesized as a function of time: (a) 12 hours; (b) 24 hours; (c) 48 hours; (d) 72 hours; (e) 96 hours.

To further understand the growth of PNW-6 crystals, we collected SEM images at higher magnification (**Error! Reference source not found.**). SEM image of the bare support (Figure 32a) indicated elongated and plate-like dense morphology. It should be noted that this bare support (Figure 32a) is not functionalized with NaOH or APTES and hence not an exact representation of the support used for synthesis. Primary observation of the 12 hours synthesis (**Error! Reference source not found.**b) shows that PNW-6 crystals are formed as isolated islands rather than continuous film as opposed to 24 and 48 hour membranes (**Error! Reference source not found.** c and d) where dense layer of PNW-6 could be identified. Comparison of the 12-hour membranes background to the bare supports' morphology however indicates that the isolated islands are indeed PNW-6 crystals and not the alumina substrate. The crystal size on the 48-hour membrane (Figure 32d) is almost double that of the 24-hour one indicating that prolonged exposure to the metal-precursor solution increased the crystal size. For the 72-hour membrane (Figure 32e), the morphology was not evident from the SEM images probably due to charging effects. The size of crystals grown are smaller than the 12-hour membrane and there also seems to be a lack of continuity. For the 96-hour membrane (Figure 32f), there is reappearance of crystallinity. The crystal sizes are comparable to 12-hour membrane. The trend where the size of crystals increases to a maximum crystal size/critical crystal size and then starts either fragmenting/breaking or re-dispersing into the solvent following by partial or full reconstruction/recrystallization (shown by reduction in crystal size) is an interesting phenomenon which can be further verified by exploring the growth kinetics of these membranes.

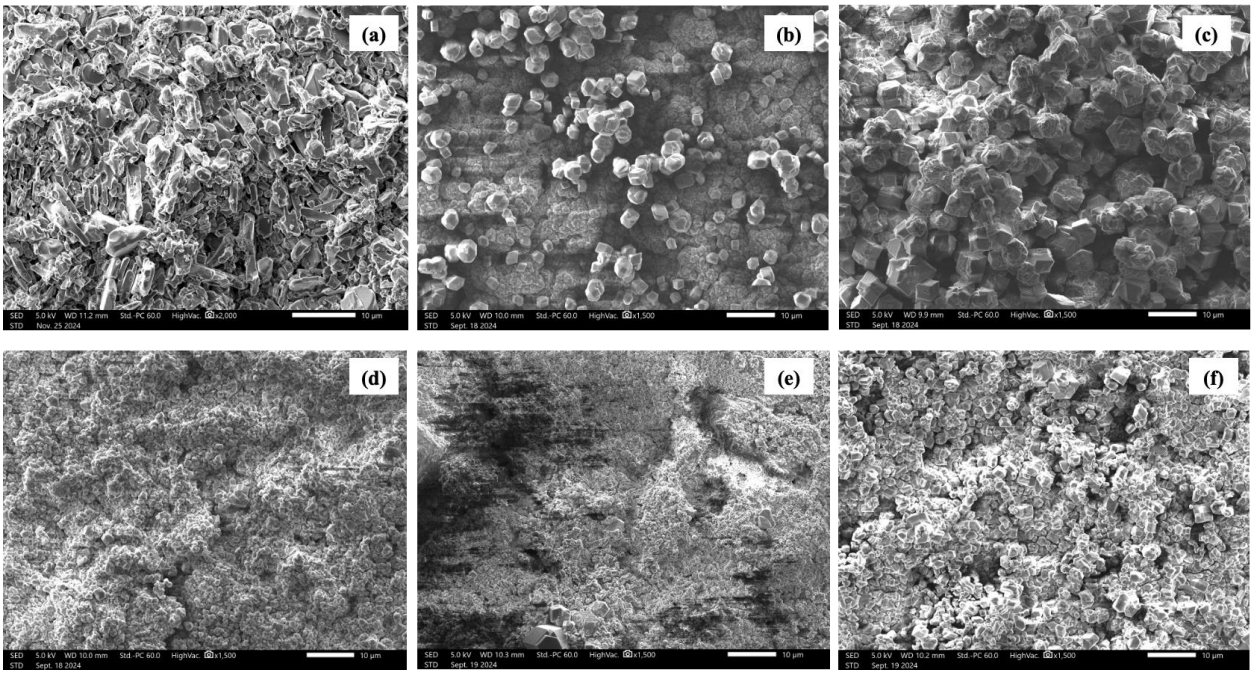

Figure 32: Top view high magnification SEM images of PNW-6 membranes synthesized as a function of time: (a) bare support; (b) 12 hours; (c) 24 hours; (d) 48 hours; (e) 72 hours; (f) 96 hours.

We then collected cross-sectional images of the membranes and is presented in Figure 33. Cross-sectional view of the bare support was collected to vividly distinguish between the membrane layer and the substrate to measure the thickness of the membrane layer. As time increased till 48 (Figure 33 d) hours, we observed an increase in thickness of the formed membrane layer. For the 72-hour membrane (Figure 33 e), the thickness of the deposited layer was inconclusive because of chargeability issues. For the 96-hour membrane (Figure 33 f) however, the thickness of the grown membrane was comparable to 12 or 24-hour membrane.

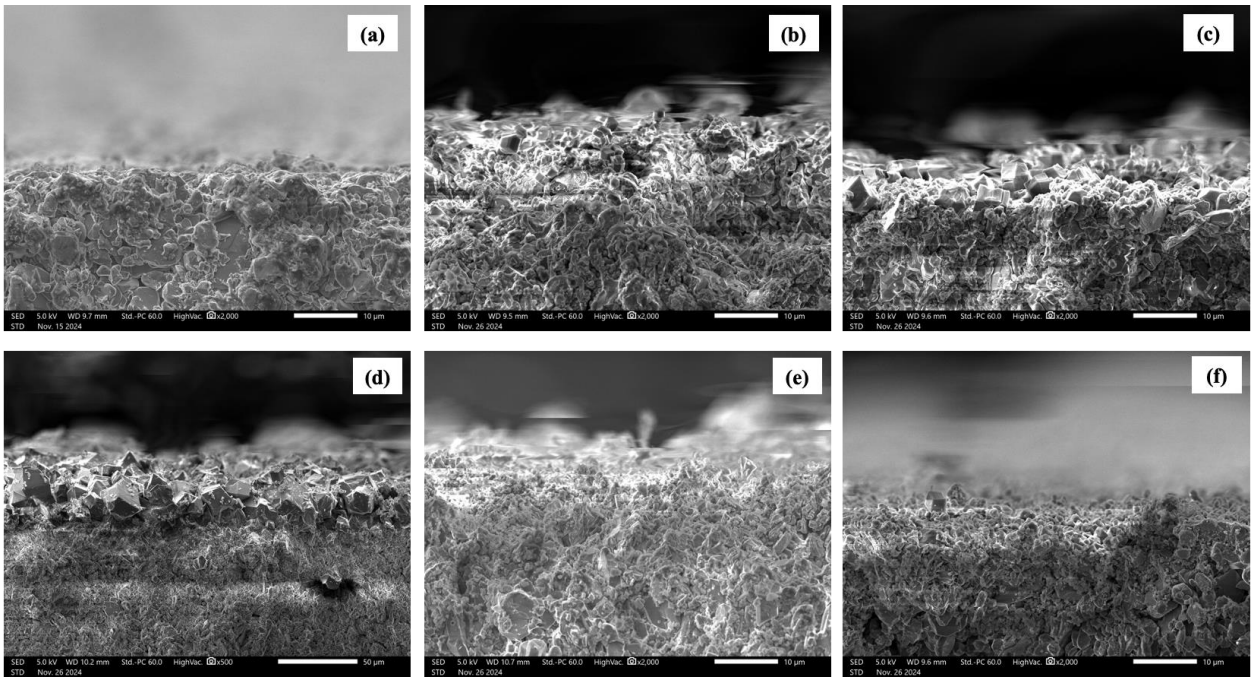

Figure 33: Cross sectional view SEM images of PNW-6 membranes synthesized as a function of time: (a) bare support; (b) 12 hours; (c) 24 hours; (d) 48 hours; (e) 72 hours; (f) 96 hours.

Top view EDS data was collected on the 48(1) membrane to see how well or not the elements are dispersed on the alumina substrate. We tracked elements that constitute the majority of PNW-6 including C, Co, Na long with the major constituents of the substrate namely Al and O. It is evident from Figure 34 that the dispersion of Co, N and C are homogeneous in the membrane, whereas the Al and O is found in sparse. This is a conformation that the support has been uniformly covered/coated with the intended material.

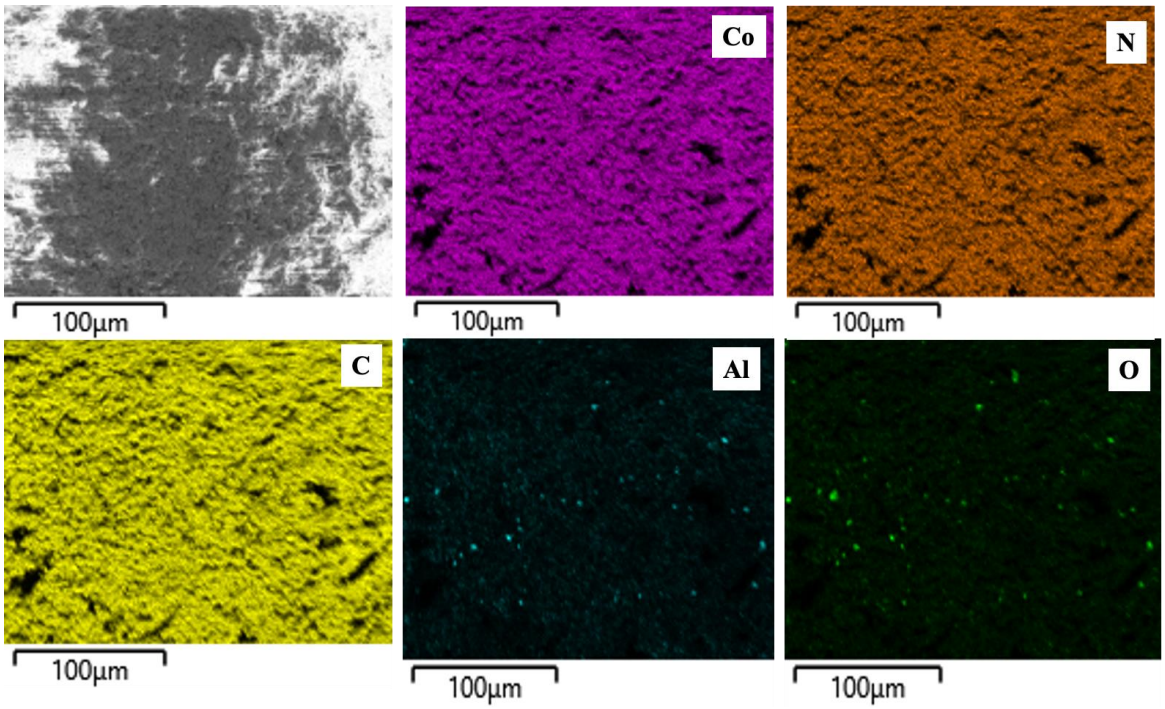

Figure 34: Top view EDS on 48(1) membrane.

We then studied the cross-sectional view EDS on the same membrane and is shown in Figure 35. It can be observed that the elements such as Co, N and C are found in sparse concentration also in the interior layers of the alumina support. We believe this could be due to penetration of the formed material or the membrane solution into the alumina substrate. This particularly emphasizes the necessity for characterization techniques such as SEM imaging with EDS.

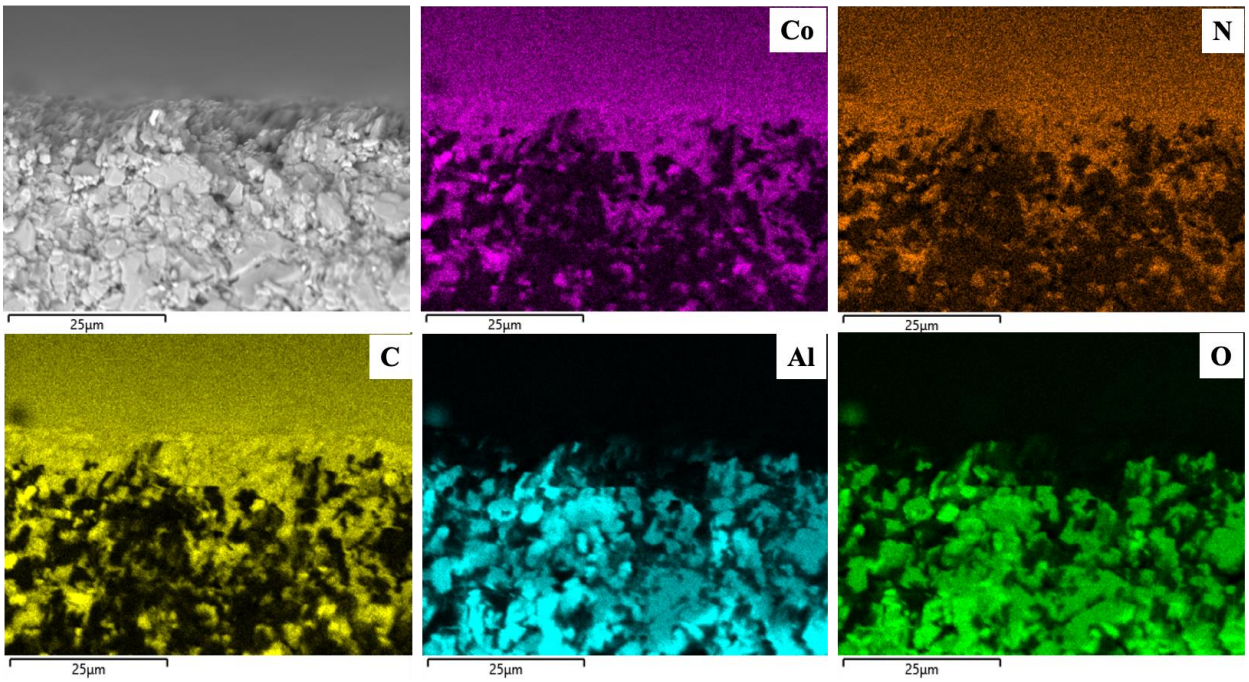

Figure 35: Cross-sectional view EDS on 48(1) membrane.

5.0 Gas permeance testing

To evaluate the separation performance of membranes, the schematic in Figure 36 was used. G1, G2, and G3 point to the three MFCs. These MFCs could be connected to pure or mixed gases to simulate any test conditions. The membrane is fit inside a membrane module made of two flanges with grooves to accommodate the support. An O-ring is used to hold the membrane in place and seal is created with the help of radial pressure. Another gasket is used on the outer circumference between the flanges. The two flanges are tightened with three sets of screws (two each on opposite sides making six in total). Once tightened, the screws create a radial seal. A back pressure regulator is connected to the retentate side of the membrane module indicated as BPR in Figure 36. Pressure relief valves are appropriately added to the retentate and permeate sides to avoid any high-pressure buildup. Mass flow meters connected on the permeate and retentate side monitor the flow rate of gases. The BPR on the permeate side is set to 14.79 psia to avoid any cross inflow of atmospheric air into the system. Most of the gases from the permeate side vents to the atmosphere while a portion of it goes to the MS. A needle valve is installed in the permeate side of the membrane connecting it to the MS. The needle valve is opened 7.5 turns to let sample gas flow to the MS. Upon initial analysis of the MS signal, we were not able to consistently obtain the same pressure readings across measurements. This could be due to two reasons. One there could be inconsistency in engaging the needle valve leading to incorrect assumption of the amount of gas flowing into the MS. Two, we observed additional N_2 signal in the MS that was otherwise missing as the analysis gas was only a blend of Ar, Xe and Kr which attested that the vent line from the permeate side of the membrane was contaminating the MS line.

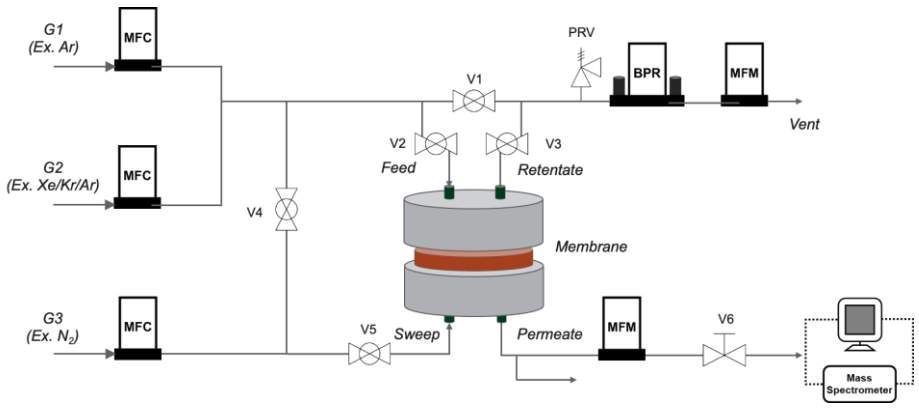

Figure 36: Schematic of membrane testing module.

To fix this issue, an additional MFC, was replaced with the needle valve. The set point of the MFC was fixed at 0.085 SCCM after multiple tests to make sure the MS is over pressurized. The membrane setup in Figure 37 was thus modified from Figure 36 from where the gas from the permeate side was vented to the room.

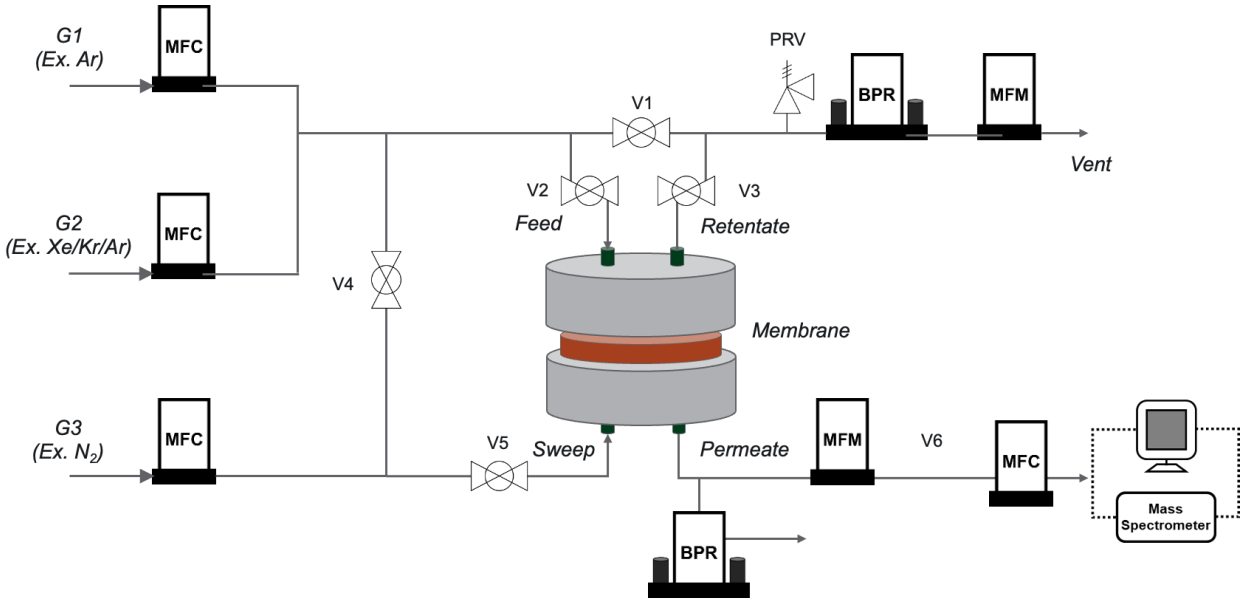

Figure 37: Modified schematic of membrane testing module.

Calibration of the membrane testing unit was essential to avoid any discrepancies since not all the measurements were collected on the same day. Prior to measuring the separation performance using any membrane, the system was calibrated using the desired gas mixture. Calibration is done bypassing the membrane module by flowing the gases from the MFCs to the MS while maintaining the MFC reading to the MS at 0.085 SCCM. To mimic different test results, different concentrations of gases are created with Ar as a diluting gas and the signals are monitored with MS. Initially, Ar is flowed at 20 SCCM creating gas concentrations of 0 ppm Xe, 0 ppm Kr and 1000000 ppm Ar. Once equilibrium is reached (when the signal of Ar is stable), analysis gas mixture (1000ppm Xe, 100ppm Kr balanced with Ar) is flown at 10 SCCM and the flow rate of Ar is reduced to 10 SCCM creating a gas concentration of 500 ppm Xe, 50 ppm Kr and 999450 ppm Ar. For the last data point, analysis gas mixture is flown at 20 SCCM and the flow rate of Ar is reduced to 0 SCCM creating a gas concentration of 1000 ppm Xe, 100 ppm Kr and 998900 ppm Ar. Pressure data collected from MS is then plotted against concentration (Figure 38) for the three gases. Slope and intercepts for each gas (inserts in Figure 38) are calculated from the calibration curves with an assumption of linear fit. This step is necessary to interpolate or extrapolate any gas concentrations that might be observed when membranes are tested.

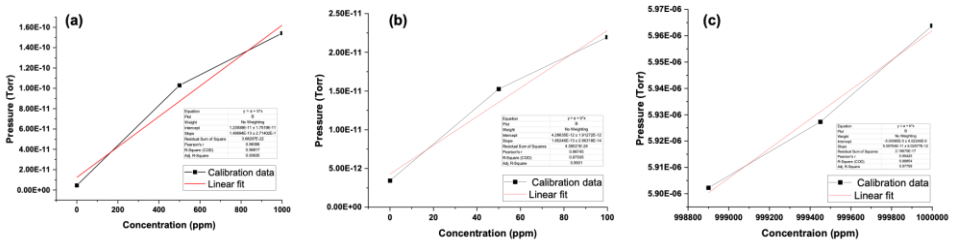

Figure 38: Calibration curves for Xe (a), Kr (b) and Ar (c).

Initially, a purge gas (N_2) is flowed through the membrane for 1 hour to clean out any impurities that could affect the separation performance. During the purging, valves V2 and V3 are open and valve V1 is closed. Valves V2 and V3 are closed and valve V1 is open after the initial purge. Once the MFCs are set to the desired flow rates, the feed pressure is set with the help of a BPR. After the feed pressure is stabilized, valves V2 and V3 are opened to let the gas flow through the membrane and the performance is monitored with the MS. No purge gas is used for this membrane performance evaluation, although there is provision to include one, if necessary, as indicated by valve V5. The pressure in the MS was monitored and maintained at approximately $6.5e^{-05}$ torr. For single gas permeance calculations (where one gas was flown at a decided flow rate), only the reading from the permeate side MFM was considered.

Knudsen diffusion selectivity is defined as:

$$\alpha_{Knudsen\frac{i}{j}} = \sqrt{\frac{M_j}{M_i}}$$

Where, M_j is the molar mass of component j and M_i is the molar mass of component i. The Knudsen diffusion selectivities for Xe, Kr and Ar along with their molar mases are given in Table 1.

Table 1: Knudsen diffusion selectivities

	Molar mass (g/mol)	Ar/Kr	Kr/Xe	Ar/Xe
Argon (Ar)	39.95	1.45	1.25	1.81
Krypton (Kr)	83.80			
Xenon (Xe)	131.29			

In this report, selectivity is defined as:

$$\alpha_{\frac{i}{j}} = \frac{y_i}{y_j}$$

Where, y_i is the permeance of gas i and y_j is the permeance of gas j as calculated from the permeate flow rate and gas concentrations.

5.1 PNW-24 membrane

Single gas permeances were collected on the PNW-24 membranes using pure Xe and Kr gases. The separation data presented in **Error! Reference source not found.** is for PNW-24 membranes with 3, 4, and 5 layers (additional layers on the same membrane). It was observed that as the number of layers increased, the permeance of Kr also increased but Xe permeance remained similar. This might be due to more material being available for Xe interaction thus retaining more Xe gas while allowing Kr to pass through. This resulted in a slight increase in selectivity of Kr over Xe. Addition of more layers on the PNW-24 membrane did alter the permeances of Xe or Kr, thus no additional layers were added. A highest Kr/Xe selectivity of 1.05 was observed after 5 layers which is closer to Knudsen diffusion selectivity (Table 1).

Table 2: Separation performance of PNW-24 membranes

	Xe permeance [10^{-7}mol/m^2·s·Pa]	Kr permeance [10^{-7}mol/m^2·s·Pa]	Kr/Xe selectivity
PNW-24-3R	30.3	24.0	0.80
PNW-24-4R	29.4	26.0	0.87
PNW-24-5R	29.8	31.0	1.03

A one-layer membrane was then chosen to study single gas permeances and ideal gas selectivities using pure He, Ar, Kr and Xe gases. The highest selectivity was observed for He/Xe of 3.4 (insert in Figure 39). This might be majorly due to the difference in kinetic diameters of He and Xe being apart by more than 2Å (x axis in Figure 39) second to the higher affinity of Xe towards the material. A highest permeance of around 7x10^{-7} mol/m^{2}sPa was observed only for He. All other gas permeances were less than 3x10^{-7} mol/m^{2}sPa which is an indication that the membrane was too thick to allow any gas to permeate through even though the pressure retention was about 20 psia.

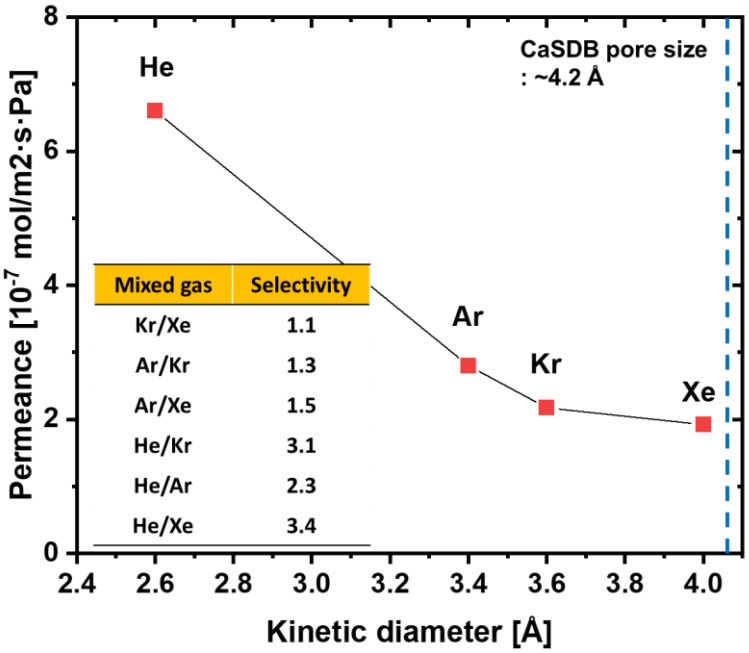

Figure 39: Single gas permeances and ideal selectivities on PNW-24 membranes.

Binary gas mixture with ratios mentioned in Table 3 (not equimolar) was then fed through this membrane to obtain the separation performance with a feed pressure of 20 psia and feed flow rate of 20 SCCM. Highest permeance was observed for Ar and He gases (Table 3) which points out that size exclusion is the dominant phenomenon for gas separation with PNW-24 membrane. Highest separation selectivity was observed for the He/Xe and He/Kr gas pairs.

Table 3: Binary gas mixture separation performance of PNW-24 membranes

Mixed gas	Xe permeance [10^{-7}mol/m^2·s·Pa]	Kr permeance [10^{-7}mol/m^2·s·Pa]	Ar permeance [10^{-7}mol/m^2·s·Pa]	He permeance [10^{-7}mol/m^2·s·Pa]	Selectivity
Xe:Kr (20%:80%)	4.37	7.95			1.80
Xe:Ar (20%:80%)	6.67		9.81		1.47
Xe:He (20%:80%)	8.48			18.9	2.23
Kr:Ar (20%:80%)		5.47	10.7		1.95
Kr:He (20%:80%)		8.75		20.0	2.29
He:Ar (20%:80%)			10.7	9.64	0.9

5.2 PNW-6 membrane

Single gas permeances were measured for the PNW-6 (HC) membrane. A Kr/Xe ideal selectivity of 3.8 was observed indicating that gas affinity plays a significant role in separating them as size exclusion would have allowed both Xe and Kr to pass through the membrane. A high Ar/Xe selectivity of 4.6 and He/Xe selectivity of 7.2 was also observed with the HC membrane. Though the high permeance of the PNW-6 (HC) membrane for all the gases is a good indication of the separation capability, its pressure retention and SEM images say otherwise. The maximum pressure that the HC membrane could retain was 15-16 psia indicating that there could be defects/cracks causing gases to pass through them rather than interacting with the material itself as gases prefer to take the path of least resistance.

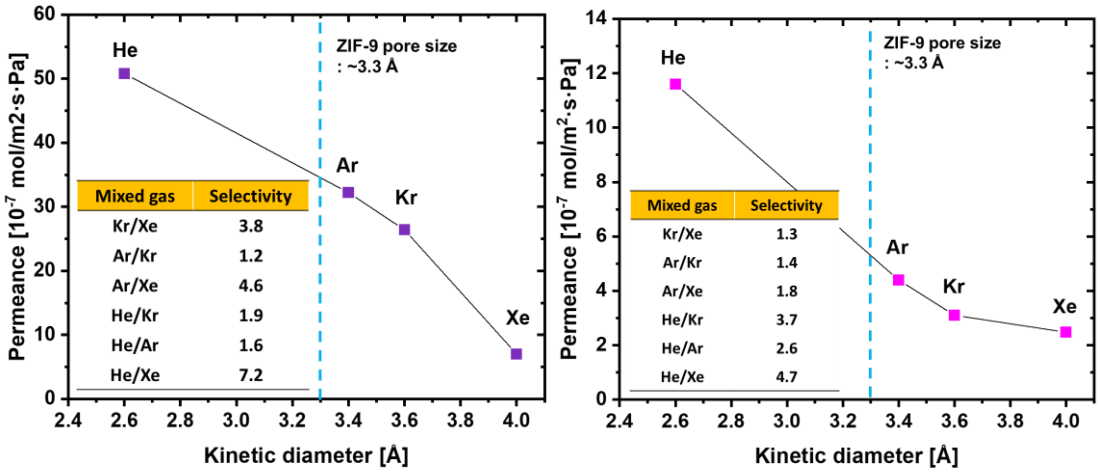

Figure 40. Single gas permeances and ideal selectivities on PNW-6 (HC) membranes (left) and PNW-6 (LC) membrane (right).

On the other hand, the LC membranes pressure retention capacity was about 19 psia indicative of no major cracks or defects which is attested by top view SEM images of the membrane. Moderate permeances and selectivity in comparison to HC membrane was observed as indicated in insert of Figure 40 (right). Binary gas separation performance of LC membrane is given in Table 4. Very high He/Xe selectivity of 33 was obtained followed by Ar/Xe and Kr/He selectivity of around 2.

Table 4: Separation performance of PNW-6 (LC) membranes: binary gases.

Mixed gas	Xe permeance [10^{-7}mol/m^2·s·Pa]	Kr permeance [10^{-7}mol/m^2·s·Pa]	Ar permeance [10^{-7}mol/m^2·s·Pa]	He permeance [10^{-7}mol/m^2·s·Pa]	Selectivity
Xe:Kr (20%:80%)	3.10	6.40			2.10
Xe:Ar (20%:80%)	9.55		21.8		2.28
Xe:He (20%:80%)	6.17			203.8	33.0
Kr:Ar (20%:80%)		18.2	18.5		1.01

Kr:He (20%:80%)	20.9		49.7	2.38
He:Ar (20%:80%)		23.6	22.0	0.90

5.3 Membrane performance under dilute conditions

Gas separation data using mixed dilute gas was collected on PNW-24, CC3, SAPO-34, SAPO-56 and PNW-6 membranes. Prior to testing, the membranes were placed in a glass petri dish inside a vacuum oven at 65°C –70°C overnight. Only the membrane intended for testing was removed and carefully placed in a plastic container with a cap and immediately taken to the testing setup to be mounted inside the membrane cell with an O-ring to create a seal. This step was taken to avoid any air exposure to the membrane. An additional step was taken by purging the membrane with pure N_2 gas to ensure any other unwanted guest molecules were expelled before analysis gas could encounter the membrane. Pure N_2 was fed at 20 SCCM flow rate with a controlled MFC set to 0.085 SCCM. The pressure in the MS controller was monitored to maintain consistently around $6x10^{-5}$ torr. After signals from all other gases flattened out to lower values as observed from the MS signal, which approximately took anywhere between an hour to an hour and a half, analysis gas (comprising of 1000ppm Xe, 100ppm Kr balanced with Ar) was flown at 20 SCCM with the same MFC set point of 0.085 SCCM. A back pressure regulator was used to control the feed pressure to the membrane. The feed pressure is dependent on the amount of material coated and the formation of membrane layer thus it is not a constant value. The analysis gas was flown until signals from all the gases plateaued which approximately took anywhere between 2 to 2.5 hours depending on test conditions. This cycle (N_2 purging followed by analysis gas) was repeated once more to get a total of two data curves for each membrane tested. To analyze the data obtained from MS, plateau regions were identified for each gas from the analysis gas run and the pressure values from that time interval was averaged. The selectivity value presented corresponds to average of two runs for each membrane tested.

Table 5: Separation performance of membranes under dilute gas conditions

Time	Xe permeance [10^{-7} mol/m^2·s·Pa]	Kr permeance [10^{-7} mol/m^2·s·Pa]	Ar permeance [10^{-7} mol/m^2·s·Pa]	Kr/Xe	Ar/Kr	Ar/Xe
SAPO-34	0.69	0.88	0.82	1.29	0.93	1.19
SAPO-56	14.08	14.47	57.43	1.03	3.97	4.08
PNW-24	12.48	13.46	10.01	1.08	0.74	0.8
CC3	12.62	10.97	60.19	0.87	5.49	4.77

For the SAPO-34 membrane, only the membrane with highest pressure retention was tested for dilute gas separation. A very low Xe, Kr and Ar permeance was observed for the SAPO-34 membrane along with selectivities very close to Knudsen selectivities as indicated in Table 1. In the case of SAPO-56 membranes, the permeances of Xe, Kr and Ar increased by a magnitude of two. The Ar permeance for the SAPO-56 membrane is 57.43 x 10^{-7}mol/m^2·s·Pa in comparison to Xe and Kr permeances at around 14 x 10^{-7}mol/m^2·s·Pa**.** These values indicate that the membrane allows more Ar to permeate in comparison to both Xe and Kr. The pore size of SAPO-56 (3.4 x 3.6 Å) being close to the kinetic diameters of both Ar and Kr, the permeation of the two gases follows the predicted behavior. On the other hand, the permeance of Xe is also very similar to Kr indicating that affinity of Xe towards the membrane also plays a critical role in gas separation. This difference in permeances of the gases lead to a moderate selectivity for Ar/Kr and Ar/Xe and a selectivity closer to Knudsen selectivity (1.03) for Kr/Xe. The current results encourage the optimization of SAPO-56 membrane as part of future work since many factors including the source of silica and amine and template removal could play a significant role on membrane performance.

Single layer PNW-24 membrane showed higher Xe and Kr permeance in comparison to Ar. Although the selectivities for the pairs of gases (Table 5 PNW-24) are close to Knudsen selectivity, the higher Xe and Kr permeance is quite interesting. PNW-24s high Xe affinity could be contributing for both adsorption and diffusion related gas permeance as opposed to Ar's. The pressure retention capacity for PNW-24 was higher than any tested membrane and this is an indication of the absence of any major defects or cracks. In the case of CC3, the pressure retention ability at the set flow rate was lower indicative of defects which could be mitigated by synthesizing more CC3 layers on the same membrane. As expected, (from the kinetic diameters of Ar, Xe, Kr and the pore size of CC3), the Ar permeance was higher than both Xe and Kr permeances. This led to a moderate Ar/Kr selectivity of 5.49 and an Ar/Xe selectivity of 4.77.

Table 6: Separation performance for PNW-6 membranes under dilute gas conditions

Time	Xe permeance [10^{-7}mol/m^2·s·Pa]	Kr permeance [10^{-7}mol/m^2·s·Pa]	Ar permeance [10^{-7}mol/m^2·s·Pa]	Kr/Xe	Ar/Kr	Ar/Xe
24	72.66	94.54	43.69	1.3	0.46	0.6
48 (1)	187.66	384.16	13.08	2.05	0.03	0.07
48(2)	27.37	32.62	13.46	1.19	0.41	0.49
48 (2)- Ir coated	39.41	99.92	13.57	2.54	0.14	0.34
48 (3)	25.26	17.02	30.45	0.67	1.79	1.21
48 (4)	28.93	33.28	11.03	1.15	0.33	0.38
72	21.43	22.01	73.71	1.03	3.35	3.44
96	36.4	44.48	64.31	1.22	1.45	1.77

The separation performance of optimized PNW-6 membranes is presented in Table 6. The pressure tolerance capacity for the 24-hour membrane was about 17 psia. The permeances of Xe and Kr were higher than Ar for the 24-hour membrane. But the selectivity for different pairs of gases were either close to Knudsen diffusion selectivity or lower. Overall, the separation efficiency of the membrane was moderate. For the 48-hour membrane, multiple membranes were synthesized to test data and synthesis reproducibility. In Table 6, 48(1) refers to the first membrane synthesized. 48(2) refers to the membrane synthesized using the same synthesis procedure as 48(1) but with increased solvent exchange time (60 hours instead of 24 hours in ethanol). 48(3) refers to the membrane where both the sides of the support were accidentally coated (because of poor wrapping technique) with PNW-6 and 48(4) refers to the membrane synthesized with the same procedure as 48(1). “48(2) Ir coated” refers to iridium coated 48(2)-membrane. To check the effect of Ir coating, the performance of 48(2)-membrane before and after Ir coating is shown in Table 6. Interestingly, for the 48(1) membrane the permeance of Xe and Kr were exceedingly a magnitude higher than Ar. Understanding of size exclusion proved invalid here since we expected Ar to pass through the membrane with a higher permeance in comparison to other gases. This could be due to competing effects from Xe and Kr adsorption and diffusion which was otherwise not observed in any other PNW-6 membrane. Further experimental studies and modelling must be performed on the 48(1)-membrane performance to understand this behavior. The 48(2) and 48(4)-membranes also showed similar trend for Xe, Kr and Ar permeances but with a reduced permeance for both Xe and Kr. While the permeance performance of the 48(2) and 48(4) membranes are similar, despite being synthesized like 48(1), its performance could not be reproduced. Ir coating on the 48(2)-membrane has increased its permeance for Xe and Kr while retaining the Ar permeance. On the other hand, the 72- and 96-hour membranes showed higher Ar permeance as expected from the molecular sieving effect. The increased permeance of 96-hour membrane could also be attributed to the microcracks present in the membrane indicated by its lower pressure tolerance.

6.0 PNW-6 Membrane Simulation

The data provided from experimental testing has expressed permeability and selectivity under specific conditions. This has allowed for extrapolation of membrane performance under simulated conditions that maybe present in a process off gas system across several membrane surface areas. Such extrapolations aid in determining the best means of implementation of these membranes.

The separation of krypton and xenon from argon gas is expressed both in terms of concentration and in recovery. The results identify which outlet of the membrane recovered more of the xenon and krypton from the membrane feed. Table 7 contains the parameters of the simulation. This is applied to three different PNW-6 test results based on the membrane growth time (24 hours, 48 hours, 72-hour and 96-hour). The different permeances for each component on each membrane are shown in Table 8.

Table 7: Simulation Parameters

Parameter	Amount	Unit
Feed rate	100	SLPM
Xe Concentration	1000	ppm
Kr Concentration	100	ppm
Ar Concentration	998900	ppm
Standard Temp	0	°C
Standard Press	1	atm
Membrane Pressure Drop	10	PSI

Table 8: Permeance Data (mol/m^2/s/Pa)

Membrane Type	Xenon	Krypton	Argon
24-hour	0.000007266	0.000009454	0.000004369
48-hour	0.000002737	0.000003262	0.000001346
72-hour	0.000002143	0.000002201	0.000007371
96-hour	0.00000364	0.000004448	0.000006431

6.1 Simulation Equations

Membrane behavior is very much a mass balance behavior and is frequently modelled by the same expressions used to model flash distillation. These work in conjunction with permeation equations to determine the concentrations such that the material balance and the permeance limitations are satisfied (Wankat 2009).

$$F_p y_{pi} = (\frac{P_i}{t_{ms}})A(P_r y_{ri} - P_p y_{pi})$$ Eq. 1

F_p = Permeate Stream Flow Rate
y_{pi} = Mol fraction of component i in the permeate stream
y_{ri} = Mol fraction of component i in the retentate stream
(P_i/t_{ms}) = Permeance of component i through the membrane
P_r = Pressure in the retentate stream
P_p = Pressure in the permeate stream
A = Membrane Surface Area

Equation 1 can be rearranged to generate a relation between the permeate and retentate side as shown in Equation 2. If a system is operating in steady state, then Equation 2 simplifies to Equation 3 since flows and pressures are held constant.

$$y_{pi} = \frac{P_r}{\frac{F_p}{\frac{P_i}{t_{ms}}A} + P_p} y_{ri}$$ Eq. 2

$$y_{pi} = K_i y_{ri}$$ Eq. 3

When Equation 3 is applied to the fundamental material balance equations shown below then Equation 4 is generated which predicts the concentration of one component in the retentate stream. A solver algorithm using Equations 4 and 2 can then adjust the permeate flow rate until the appropriate composition is reached based on material balance. Recoveries are calculated based on concentrations of each component in the permeate and retentate streams.

$$y_{ri} = \frac{y_{fi}}{1+(K_i-1)*A}$$ Eq. 4

Summation of Mol Fractions within any given stream:

$$1 = \sum y_i$$

Material Balance (single compound):

$$Accumulation = \sum Inputs - \sum Outputs + \sum Generations - \sum Consumptions$$

No chemical reactions are known to occur within the test apparatus which means both the sum of the generation reactions and the sum of the consumption reactions are equal to zero. Since accumulation is not significant in a membrane system then accumulation is assumed to be zero and the sum of the inputs must equal the sum of the outputs. This is similar to fundamental accounting principles but applied to physical matter instead of currency. The results from simulation experiments are presented in Figure 41-Figure 49.

6.2 Simulation Results

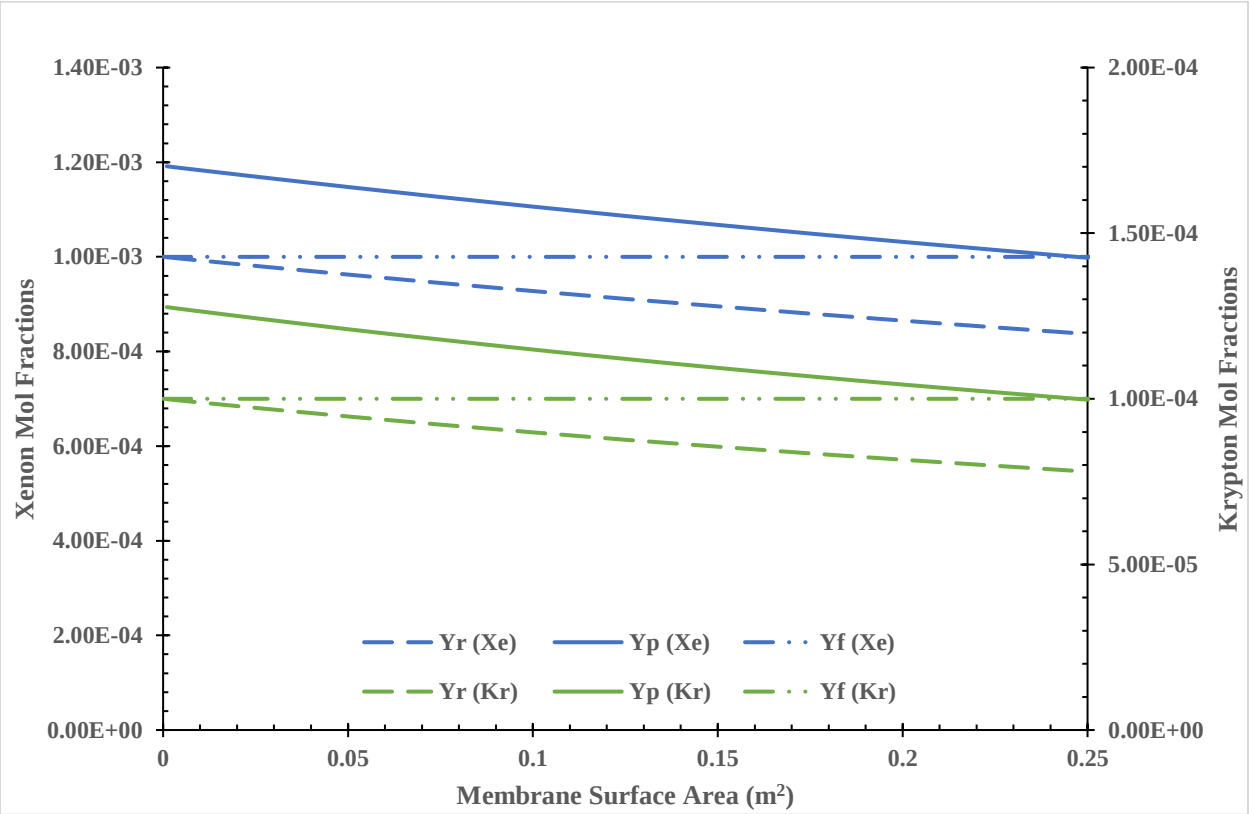

Figure 41: 24-hour PNW-6: Xe, Kr concentrations with respect to membrane area

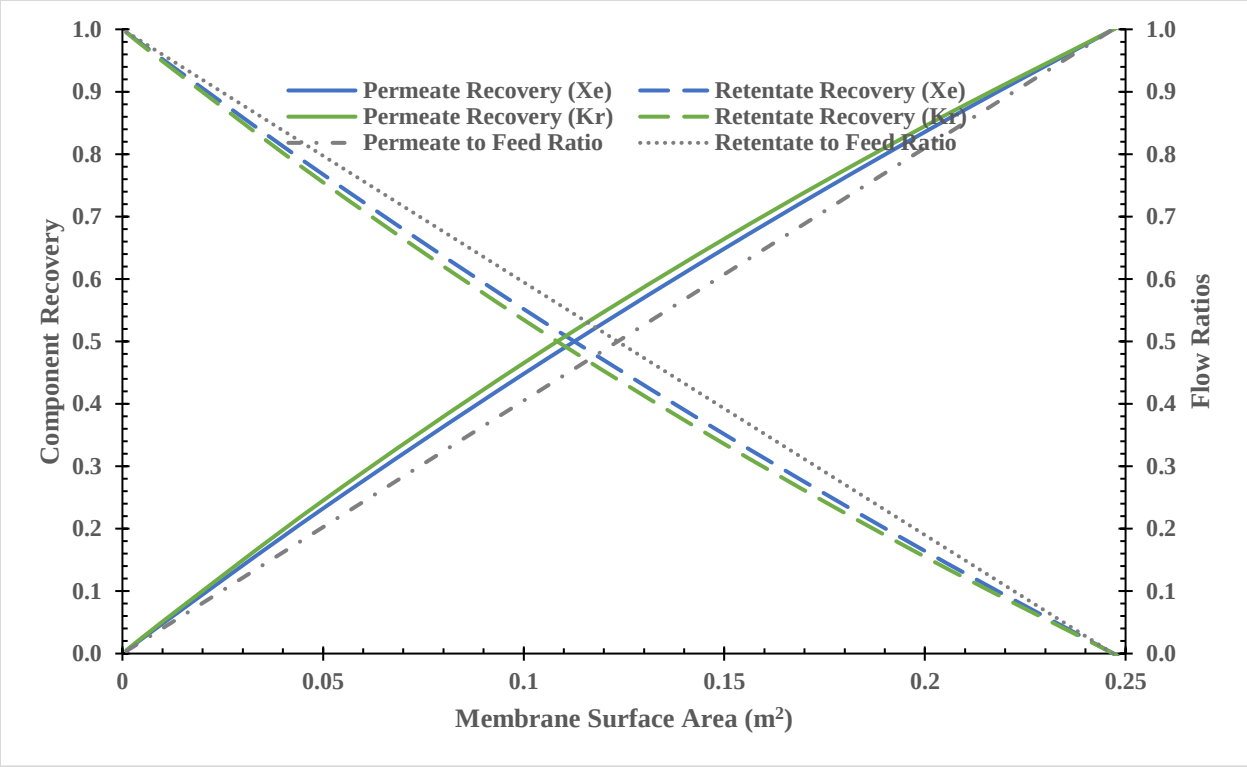

Figure 42: 24-hour PNW-6: recoveries and flow ratios with respect to membrane area

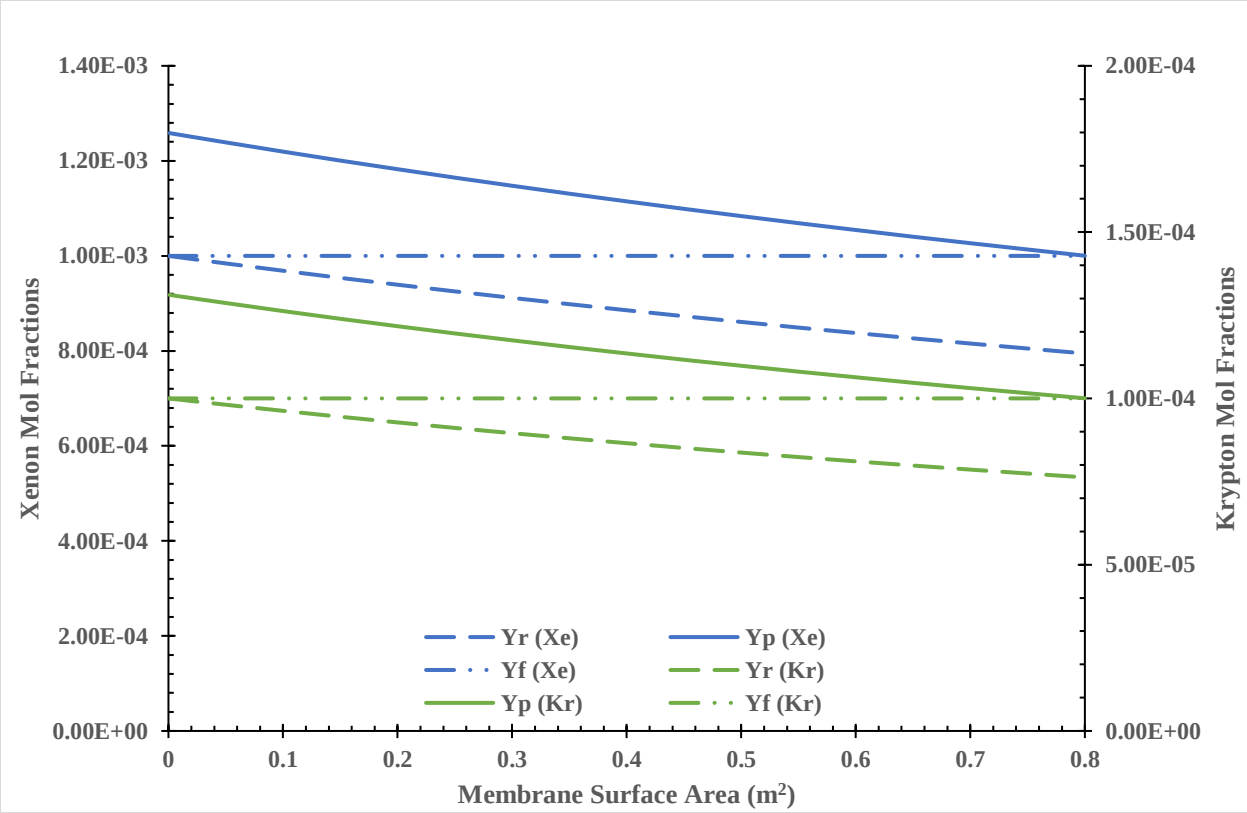

Figure 43: 48-hour PNW-6: Xe, Kr concentrations with respect to membrane area

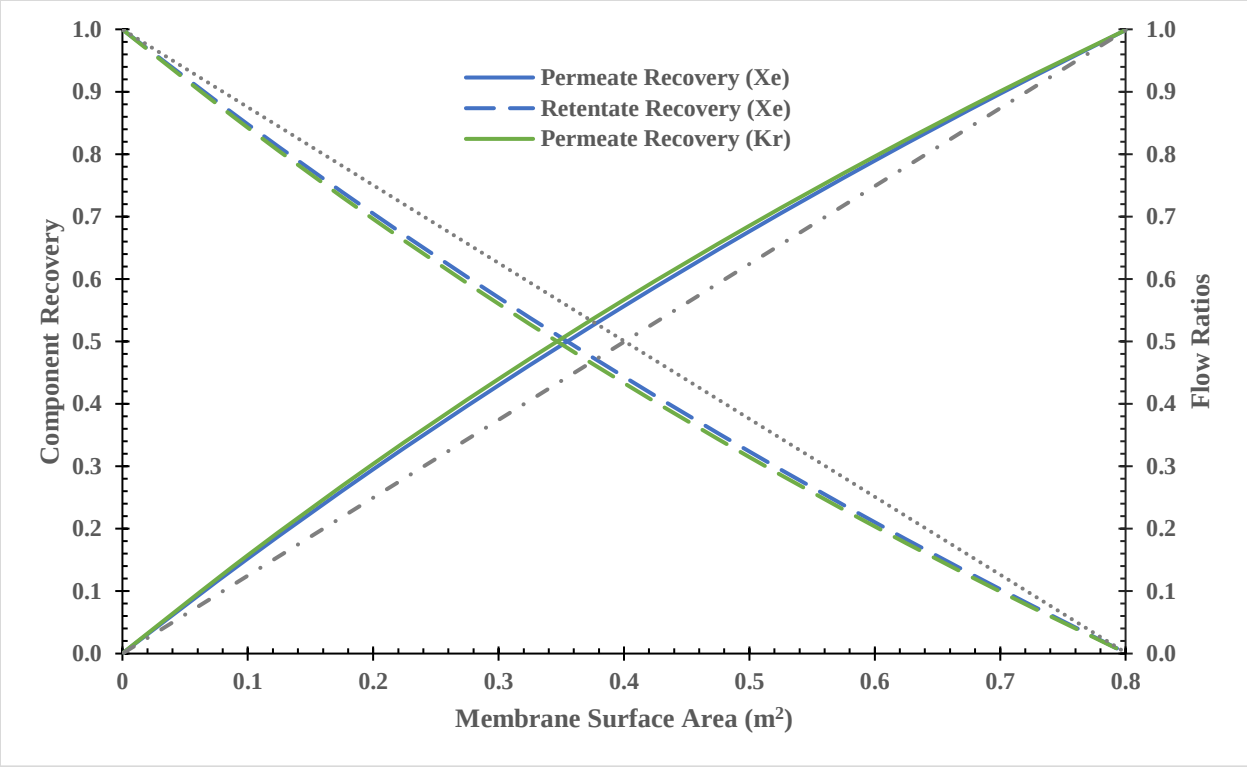

Figure 44: 48-hour PNW-6: recoveries and flow ratios with respect to membrane area

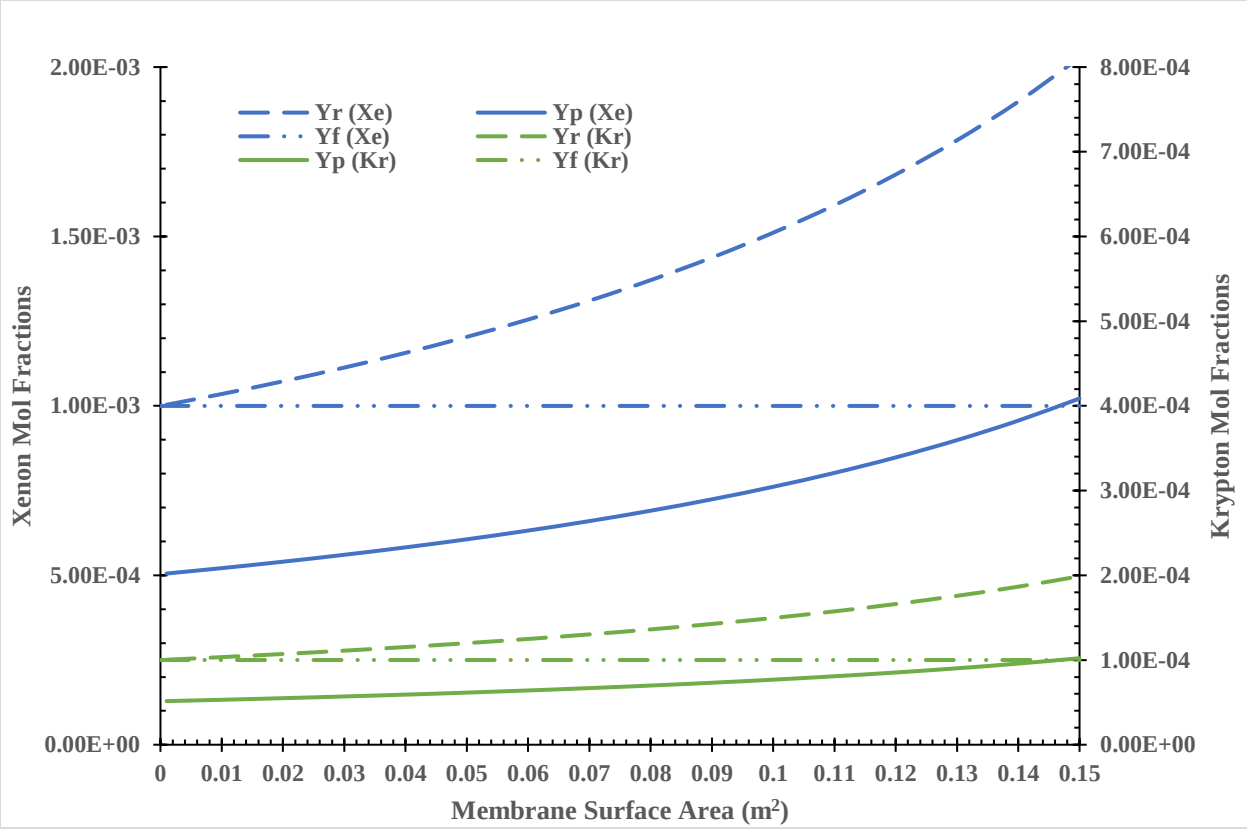

Figure 45: 72-hour PNW-6: Xe, Kr concentrations with respect to membrane area

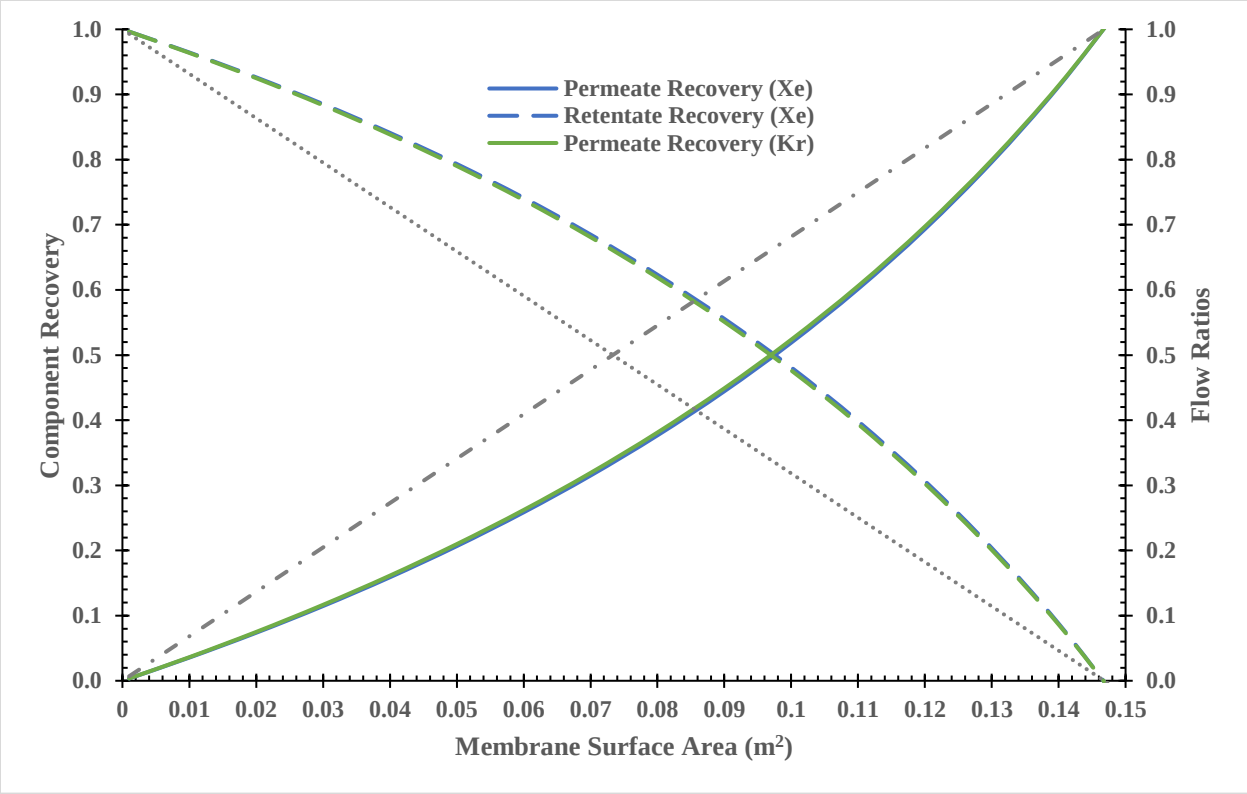

Figure 46: 72-hour PNW-6: recoveries and flow ratios with respect to membrane area

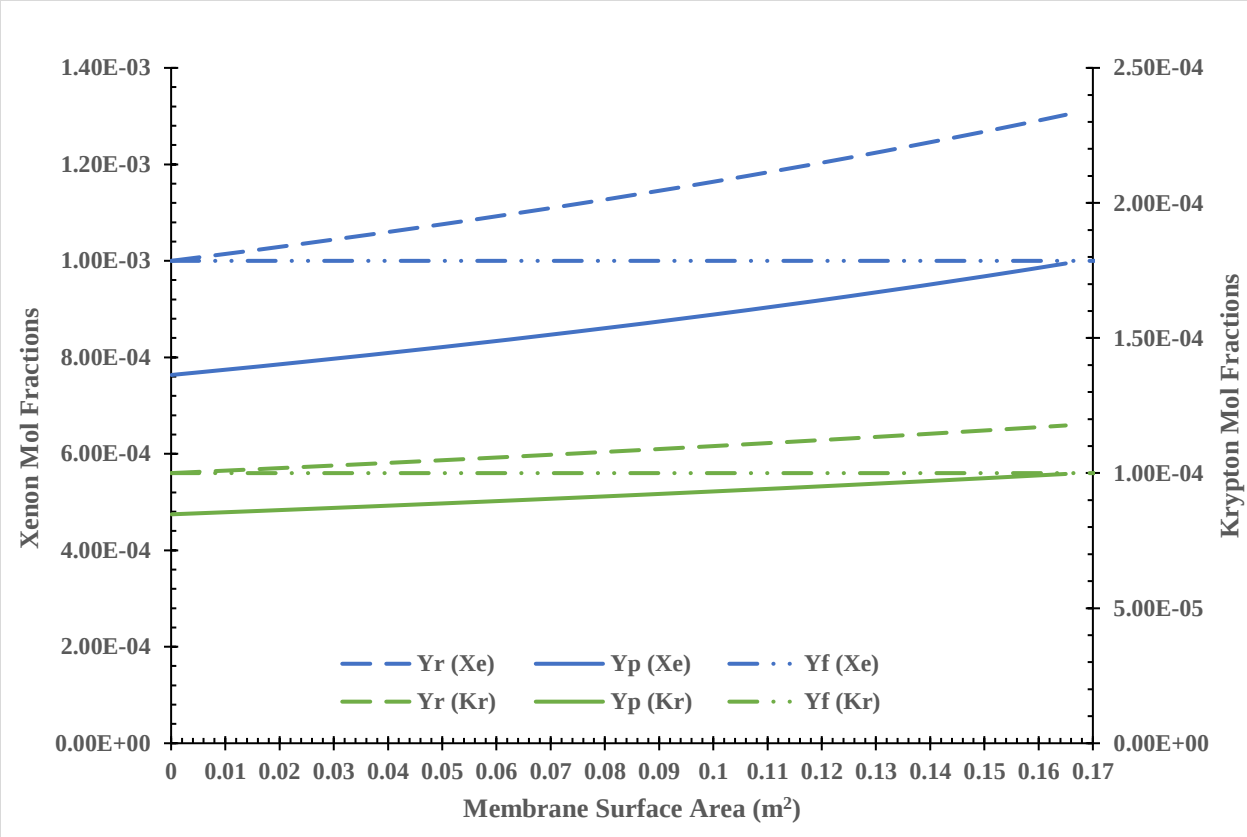

Figure 47: 96-hour PNW-6: Xe, Kr concentrations with respect to membrane area

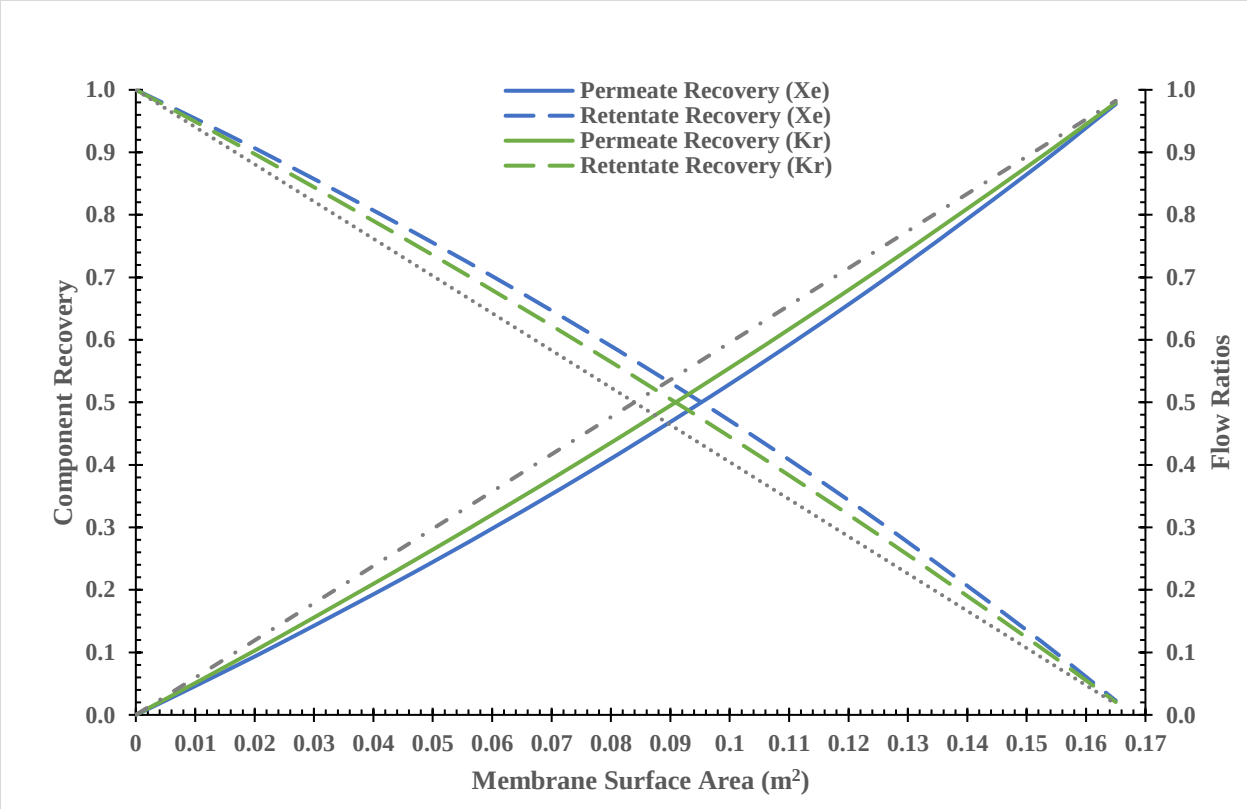

Figure 48: 96-hour PNW-6: recoveries and flow ratios with respect to membrane area

In all samples tested, a degree of separation is observable and a split between retentate and permeate streams is present. However, membrane samples with greater permeance differences between the gas components were able to achieve higher concentration changes and therefore higher separations. Also, when the gas permeances are dis-similar, the recovery fraction lines will be dis-similar to the bulk flow ration lines. The membrane that has demonstrated the highest separation is the 72 hour PNW-6 sample. This is interesting as this is the membrane with the smallest crystal size. Such crystal sizes do affect tortuosity and channel diameter of the membrane pores. This drives the permeation mechanism towards Knudsen and surface adsorption diffusion which are inherently slower than bulk flow or bulk diffusion mechanisms. Knudsen and surface adsorption diffusion are also more likely for polarizable molecules with large kinetic diameters. Since these properties are more fitting to krypton and xenon that to argon, it is sensible that krypton and xenon would move slower than argon in the 72 hour PNW-6 membrane. In the 96- and 48-hour PNW-6 membranes, the crystal sizes are larger which diminishes these effects. With the 24 hour PNW-6 membrane there were indications that the material had not coated the surface entirely which may mean these results will not extrapolate well. .

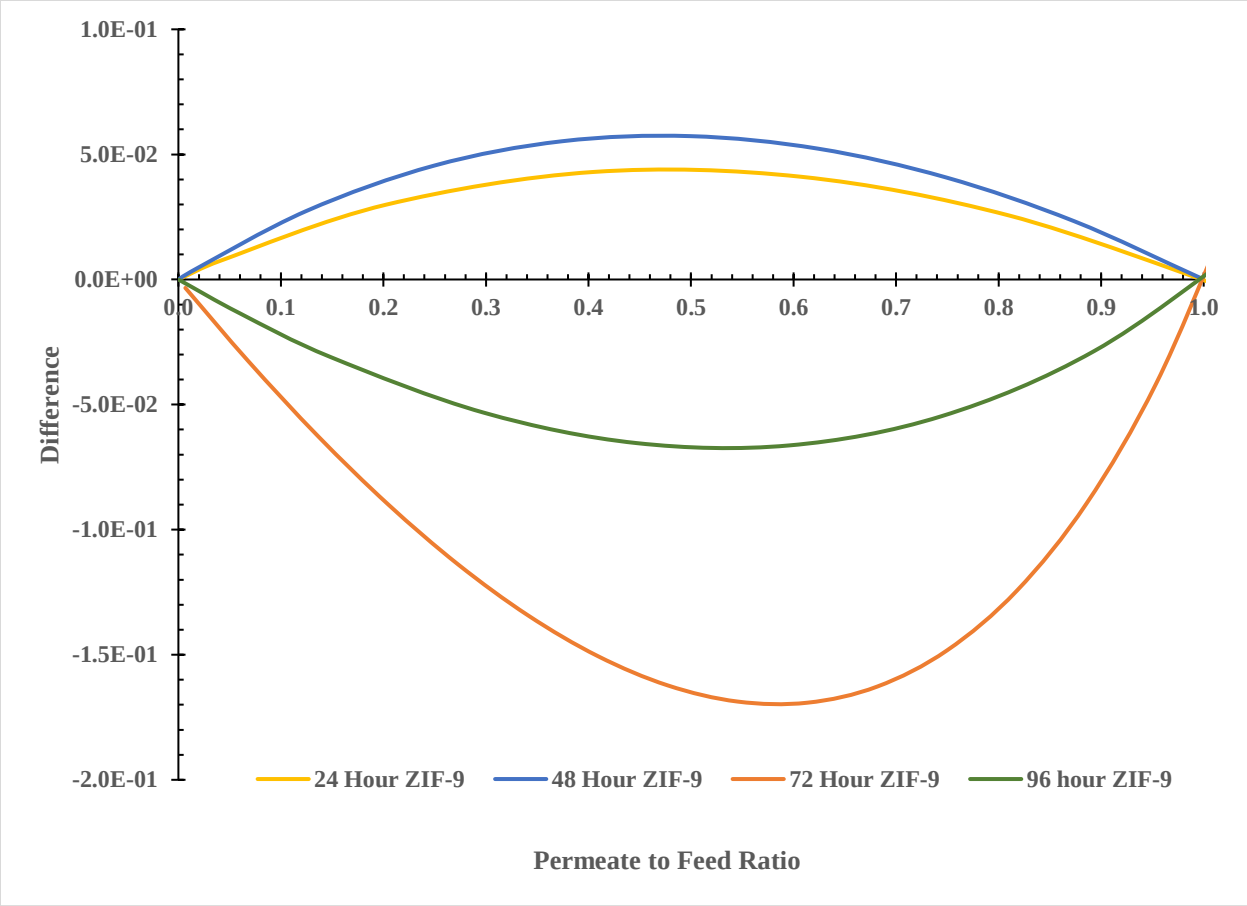

Figure 49: Difference between Xe permeate recovery and permeate to feed ratio

The difference plot shown in Figure 49 is a demonstration of the separation abilities of each lab grown membrane. The 24 hour and 48-hour membranes demonstrate weak separation capabilities since the xenon recovery in the permeate side is close to the permeate to feed ratio. This indicates that the membrane is not favoring the movement of any compound through the membrane, negating the intent of a membrane. The 72-hour PNW-6 and 96-hour PNW-6 membranes demonstrate some separation capabilities with preference to smaller crystal development on the substrate.

7.0 Cost Estimate

The pumping power requirement is also estimated and a conservative operating cost fraction of 5% is used to estimate the total operational cost the membrane into the simulated conditions. The operational cost for all membranes is considered the same since the basis is pumping power and none of the parameters affecting pumping power change with different membranes. This is likely a conservative estimate as the primary expenditure of operating a membrane is the pump pressurizing the membrane. Table 9 cost calculations for a system operating under the conditions described in Table 7.

Table 9: Operating Cost Estimate

Pump Inlet Volume	0.00167	m^3/s
Pump Outlet Volume	0.00108	m^3/s
Change in Volume	0.000584	m^3/s
Pressure change	10	PSIG
Compression Power loss	40.3	W
Fluid Movement Loss	74.7	W
Total Pump Power	115	W
Total Motor Power	230	W
Daily Energy Consumption	5.52	KWHr/day
Price of Electrical Power	$0.15	$/KWHr
Pump Cost	$0.83	$/day
Pump Cost Fraction	5%	
Daily Operational Cost	$16.55	$/day
Annual Operational Cost	$6,039.81	$/year

The annual cost is fixed due to the simulation being fixed upon a pressure and flow rate. The low cost is also associated with the fact that this is a low pressure and low flow rate system which only requires a minimal cost to operate compressors. When higher pressures or flow rates are being assumed then the cost will scale in proportion to the scale up of energy consumption to operate the compressor/pump.

8.0 Challenges and future work

- Synthesis of continuous and defect free membranes were a challenge while keeping in mind the optimization of synthesis time, concentration of precursors as well as synthesis temperature.

- For the PNW-6 membranes, additional functionalization with NaOH and APTES were necessary since we were unsuccessful in synthesizing them (we did not observe any PNW-6 crystal deposition) directly on the porous substrate. The functionalization step could be modified to reduce the overall synthesis time.

- With just imparting the OH functionality, we were still able to achieve a coating of PNW-6 on the substrate. But the separation performance and the pressure tolerance of the membrane was not as good as the APTES functionalized one.

- In the case of SAPO membranes, the time necessary to prepare the membrane solution was 4 days followed by a longer synthesis time. We intend to optimize this as part of future work by co- mixing all the precursors and letting them homogenize. The pressure retention capability of the SAPO-34 membrane was very low (15 -15.5 psia) indicating defects in the membrane synthesized. Ways to improve stability include adding more layers onto the existing membrane and optimizing the synthesis conditions.

- During our initial runs, we used a needle valve to slowly bleed the permeate side gas to the MS. We realized from our calculations that the data collected for the same membrane in two different days were not matching even though no modification had been made on the membrane. We believe this is due to the inconsistency in the needle valve engagement. To rectify this, we installed a low range MFC on the permeate side of the membrane and set it to a constant value. We observed after the installation that the signals from MS remained consistent.

- For future experiments, a purge gas could also be used in the permeate side to help carry the gases with better consistency. The purge gas could also help maintain the pressure on the permeate side at the set 14.7 psia with a regulated gas flow.

- Each membrane testing required at least 6 hours since we purged the membrane at room pressure and room temperature with N_2 as a clean-up gas for an hour followed by flowing the analysis gas until equilibrium was reached as observed with the MS signal. To reduce the time required for analysis, higher flow rate could be used for membrane testing although this may result in not allowing the gases to interact well with the membrane material.

- One side of the alumina support is wrapped with a Teflon tape to facilitate membrane growth only on one side and to increase the gas permeance after membrane interaction. We found from our experiments that if the Teflon tape is not completely wrapped or not wrapped tight enough, there could be crystals growing on the opposite side of the support non uniformly. As a solution, a wider Teflon tape could be used, or the support can be wrapped in opposite direction to ensure complete seal/coverage. A vertical

approach commonly used for synthesizing membranes could be implemented since this ensures intergrowth with the support and not just precipitated deposit of the formed PNW-6 crystals.

- Optimization is an essential step to get the best out of any process. Thus, we intend to incorporate the experimental data into a model where, either series of membranes or a combination of membrane and an adsorption column could be used to achieve a better separation.

9.0 References

Banerjee, Debasis, Cory M Simon, Anna M Plonka, Radha K Motkuri, Jian Liu, Xianyin Chen, Berend Smit, John B Parise, Maciej Haranczyk, and Praveen K Thallapally. 2016. "Metal–organic framework with optimally selective xenon adsorption and separation." *Nature Communications* 7 (1):ncomms11831.

Bernardo, Paola, Enrico Drioli, and Giovanni Golemme. 2009. "Membrane gas separation: a review/state of the art." *Industrial & engineering chemistry research* 48 (10):4638-4663.

Carreon, Moises A., Shiguang Li, John L. Falconer, and Richard D. Noble. 2008. "Alumina-Supported SAPO-34 Membranes for CO2/CH4 Separation." *Journal of the American Chemical Society* 130 (16):5412-5413. doi: 10.1021/ja801294f.

Chen, Linjiang, Paul S Reiss, Samantha Y Chong, Daniel Holden, Kim E Jelfs, Tom Hasell, Marc A Little, Adam Kewley, Michael E Briggs, and Andrew Stephenson. 2014. "Separation of rare gases and chiral molecules by selective binding in porous organic cages." *Nature materials* 13 (10):954-960.

Cheung, Ocean, Qingling Liu, Zoltán Bacsik, and Niklas Hedin. 2012. "Silicoaluminophosphates as CO2 sorbents." *Microporous and Mesoporous Materials* 156:90-96. doi: https://doi.org/10.1016/j.micromeso.2012.02.003.

Denayer, Joeri F. M., Lisa I. Devriese, Sarah Couck, Johan Martens, Ranjeet Singh, Paul A. Webley, and G. V. Baron. 2008. "Cage and Window Effects in the Adsorption of n-Alkanes on Chabazite and SAPO-34." *The Journal of Physical Chemistry C* 112 (42):16593-16599. doi: 10.1021/jp804349v.

Gan, Guoqiang, Shiying Fan, Xinyong Li, Zhongshen Zhang, and Zhengping Hao. 2023. "Adsorption and membrane separation for removal and recovery of volatile organic compounds." *Journal of Environmental Sciences* 123:96-115.

Hayashi, Hideki, Adrien P. Côté, Hiroyasu Furukawa, Michael O'Keeffe, and Omar M. Yaghi. 2007. "Zeolite A imidazolate frameworks." *Nature Materials* 6 (7):501-506. doi: 10.1038/nmat1927.

Huang, Yuyao, Dahuan Liu, Ziping Liu, and Chongli Zhong. 2016. "Synthesis of Zeolitic Imidazolate Framework Membrane Using Temperature-Switching Synthesis Strategy for Gas Separation." *Industrial & Engineering Chemistry Research* 55 (26):7164-7170. doi: 10.1021/acs.iecr.6b01290.

Li, Qiming, and Hern Kim. 2012. "Hydrogen production from NaBH4 hydrolysis via Co-PNW-6 catalyst." *Fuel Processing Technology* 100:43-48. doi: https://doi.org/10.1016/j.fuproc.2012.03.007.

Liu, Guangyu, Peng Tian, Jinzhe Li, Dazhi Zhang, Fan Zhou, and Zhongmin Liu. 2008. "Synthesis, characterization and catalytic properties of SAPO-34 synthesized using diethylamine as a template." *Microporous and Mesoporous Materials* 111 (1):143-149. doi: https://doi.org/10.1016/j.micromeso.2007.07.023.

Liu, Jiaqin, Chuanyao Liu, and Aisheng Huang. 2020. "Co-based zeolitic imidazolate framework PNW-6 membranes prepared on α-Al2O3 tubes through covalent modification for hydrogen separation."

International Journal of Hydrogen Energy 45 (1):703-711. doi: https://doi.org/10.1016/j.ijhydene.2019.10.230.

Lucero, Jolie M, and Moises A Carreon. 2020. "Separation of light gases from xenon over porous organic cage membranes." *ACS applied materials & interfaces* 12 (28):32182-32188.

National Academies of Sciences, Engineering, and Medicine. 2019. "A Research Agenda for Transforming Separation Science."

Noguera-Díaz, Antonio, Nuno Bimbo, Leighton T. Holyfield, Ibbi Y. Ahmet, Valeska P. Ting, and Timothy J. Mays. 2016. "Structure–property relationships in metal-organic frameworks for hydrogen storage." *Colloids and Surfaces A: Physicochemical and Engineering Aspects* 496:77-85. doi: https://doi.org/10.1016/j.colsurfa.2015.11.061.

Poshusta, Joseph C., Vu A. Tuan, John L. Falconer, and Richard D. Noble. 1998. "Synthesis and Permeation Properties of SAPO-34 Tubular Membranes." *Industrial & Engineering Chemistry Research* 37 (10):3924-3929. doi: 10.1021/ie980240b.

Tozawa, Tomokazu, James TA Jones, Shashikala I Swamy, Shan Jiang, Dave J Adams, Stephen Shakespeare, Rob Clowes, Darren Bradshaw, Tom Hasell, and Samantha Y Chong. 2009. "Porous organic cages." *Nature materials* 8 (12):973-978.

Wankat, Philip C. 2009. *Separation Process Engineering*. 2 ed: Prentice hall.

Wilson, Steve T., Robert W. Broach, C. Scott Blackwell, Charles A. Bateman, Nancy K. McGuire, and Richard M. Kirchner. 1999. "Synthesis, characterization and structure of SAPO-56, a member of the ABC double-six-ring family of materials with stacking sequence AABBCCBB." *Microporous and Mesoporous Materials* 28 (1):125-137. doi: https://doi.org/10.1016/S1387-1811(98)00293-5.

Wu, Ting, Xuhui Feng, Maria L. Carreon, and Moises A. Carreon. 2017. "Synthesis of SAPO-56 with controlled crystal size." *Journal of Nanoparticle Research* 19 (3):93. doi: 10.1007/s11051-017-3772-3.

Pacific Northwest National Laboratory

902 Battelle Boulevard
P.O. Box 999
Richland, WA 99354

1-888-375-PNNL (7665)

www.pnnl.gov